SPEC inc

3022 Sterling Circle – Suite 200, Boulder, CO 80301

(303) 449-1105 (303) 449-0132 (fax)

www.specinc.com

Final Report

Fall 2015

Under DOE Award No. DE-SC0007035

Program Manager: Dr. Ashley D. Williamson

"Using Statistical Comparisons between SPartICus Cirrus Microphysical Measurements, Detailed Cloud Models, and GCM Cloud Parameterizations to Understand Physical Processes Controlling Cirrus Properties and to Improve the Cloud Parameterizations"

Principal Investigators: R. Paul Lawson, Eric Jensen

Co-Investigators: Leonard Pfister, Hugh Morrison

Sara Lance, Qixu Mo, Sarah Woods, Colin Gurganus

Report Number: DOE-SPEC-120115

Table of Contents

Executive Summary:

The dual objectives of this project were improving our basic understanding of processes that control cirrus microphysical properties and improvement of the representation of these processes in the parameterizations. A major effort in the proposed research was to integrate, calibrate, and better understand the uncertainties in all of these measurements.

Research focused on the following project objectives:

i) Algorithm development and assessment of measurement biases for the in-situ cloud probe observations during SPartICus, which are the primary measurements used for validating and constraining remote sensing and modeling results.

ii) Classification of cirrus particle habits and size distributions for the three cirrus temperature regimes used in the Jensen et al. (2013) temperature curtain statistical analysis.

iii) Classification of cirrus particle habits and size distributions based on atmospheric state (large-scale dynamics) conditions quantified by Muhlbauer et al. (2013) using clustering analysis.

Accomplishments:

- Evaluation of 2D-S data processing algorithms, and evaluation of limitations for the currently available algorithms to clouds of interest for SPartICus
- Development, testing, and implementation of new 2D-S algorithms
- Testing of instrument and algorithm performance in SPECcalibration facility.
- Experimental verification of the theoretically determined 2D-S Depth of Field
- Experimental verification of 2D-S sizing response to water droplets
- Classification of cirrus particle habits and size distributions as a function of temperature and atmospheric state.

Changes in key personnel and Implications:

Dr. Brad Baker is no longer employed by SPEC, Inc and has contributed to this project as a contractor on an intermittent basis. Drs. Sara Lance and Colin Gurganus took over the work that Dr. Baker was expected to perform at SPEC, but additional time was required to gain familiarity with the SPEC data analysis software and instrumentation after their hires in May 2012 and March 2015. A number of problems with how the data was originally processed were discovered along the way, and intermediate datasets were provided to the community in the interim while new algorithms were developed.

Products/Publications/Conference Papers:

Through supply of revised archived data products, user-customized data products specific to a particular investigation, discussion, analysis feedback, and other contributions, SPEC personnel had involvement in the following publications and conference presentations:

Atlas, R., A. M. Fridland, E. J. Moyer, P. Lawson, G. M. McFarquhar, J. Um, G. S. Diskin, H Kalesse, 2013: Using SPartICus measurements to study ice particle size distribution modes within in situ cirrus, AGU Annual Meeting.

Bardeen, C. G., A. Gettelman, E.J. Jensen, A. Heymsfield, A.J. Conley, J. Delanoe, M. Deng, and O.B. Toon, 2013: Improved cirrus simulations in a general circulation model using CARMA sectional microphysics, *J. Geophys. Res. Atmos.,* 118, 11679-11697.

Deng, M., G. G. Mace, Z. Wang, R. P. Lawson, 2013: Evaluation of Several A-Train Ice Cloud Retrieval Products with In Situ Measurements Collected during the SPARTICUS Campaign. *J. Appl. Meteor. Climatol.*, **52**, 1014–1030. doi: http://dx.doi.org/10.1175/JAMC-D-12-054.1

Erfani, E. and D. Mitchell, 2015: Developing and Bounding Ice Particle Mass- and Area-dimension Expressions For Use in Atmospheric Models and Remote Sensing, submitted to *J. Geophys. Res.*.

Jackson, R., 2016: Assessing the dependence of bulk ice properties from probes with anti-shatter tips on environmental conditions, Ph.D. Dissertation, University of Illinois at Urbana-Champaign, http://hdl.handle.net/2142/78295.

Jackson, R., G. McFarquhar, A. Fridlind, R. Atlas, 2015: The dependence of cirrus gamma size distributions expressed as volumes in N_o-λ-μ phase space and bulk cloud properties on environmental conditions: Results from the Small Ice Particles in Cirrus Experiment (SPARTICUS), *J. Geophys. Res. Atmos.*, 120, 10351-10377.

Järvinen, E., and co-authors, 2016: Spherical ice in convective clouds. Submitted to: *J. Atmos. Sci*.

Jensen, E. J., R. P. Lawson, J. W. Bergman, L. Pfister, T. P. Bui, C. G. Schmitt, 2013: Physical processes controlling ice concentrations in synoptically forced, midlatitude cirrus, *J. Geophys. Res. Atmos.*, 118, 5348-5360.

Jensen, E. J., P. Lawson, L. Pfister, P. Bui, J.W. Bergman, and C.G. Schmitt, 2012: Using Statistical Comparisons Between Simulations and Observations to Understand Physical Processes Controlling Midlatitude Cirrus Ice Concentrations, AGU Annual Meeting.

Lance, S., P. Lawson, E. Jensen, A. Mulbauer, 2013: SPARTICUS and MACPEX Cirrus Particle Sizes and Habits as a Function of Temperature and Synoptic Cirrus Type, AGU Annual Meeting.

Lawson, R.P.: Effects of ice particles shattering on the 2D-S probe, 2011: *Atmos. Meas. Tech*., 4, 1361-1381.

Lawson, P., S. Lance, Q. Mo, and E. Jensen, 2013 Poster presentation, SPartICus Cirrus Particle Sizes and Habits, Annual ASR 2013 meeting.

Liu, X., K. Zhang, J. Comstock, H. Wan, M. Wang, 2013: Investigating the Impact of Updraft Velocity on Cirrus Cloud Properties Using the CAM5 Model Constrained with Field Measurements, AGU Annual Meeting.

Liu, X., X. Shi, K. Zhang, E.J. Jensen, A. Gettelman, D. Barahone, A. Nenes, and P. Lawson, 2012: Sensitivity studies of dust ice nuclei effect on cirrus clouds with the Community Atmosphere Model CAM5, *Atmos. Chem. Phys.*, 12, 12061-12079.

Luebke, A.E., A. Afchine, A. Costa, J. Meyer, C. Rolf, N. Spelten, L.M. Avallone, D. Baumgardner, and M. Kramer, 2015: The origin of midlatitude ice clouds and the resulting influence on their microphysical properties, submitted to *Atmos. Chem. Phys. Discuss.*, 15, 34243-34281.

McFarquhar, G.M., J. Um, T. Hsieh, M. Freer, B.F. Jewett, J. Mascio, S. Kim, K. Yaffe, T. Nousiainen, J. Tiira, H. Hindqvist, A. Schwarzenboeck, and A. Delplanque, 2013: Use of In-Situ Cloud Probe Data to Derive Bulk Cloud Paremeters and Their Uncertainties: Impacts for Models and Remote Sensing Retrievals, AGU Annual Meeting.

Mishra, S., D. L. Mitchell, D. D. Turner, and R. P. Lawson, 2014: Parameterization of ice fall speeds in midlatitude cirrus: Results from SPartICus, *J. Geophys. Res. Atmos.*, 119, 3857–3876, doi:10.1002/2013JD020602.

Mitchell, D. L., M. Avery, A. Garnier, 2014: Inferred Differences in Ice Crystal Nucleation Rates between Continental and Maritime Deep Convective Clouds, AGU Annual Meeting.

Muhlbauer, A., T.P. Ackerman, J. Comstock, G. Diskin, S.M. Evans, P. Lawson, and R.T. Marchand, 2014: Impact of large-scale dynamics on the microphysical properties of mid-latitude cirrus, *J. Geophys. Res. Atmos.*, 119, 3976-3996.

Muhlbauer, A., T.P. Ackerman, R.P. Lawson, S. Xie, Y. Zhang, 2015: Evaluation of cloud-resolving model simulations of midlatitude cirrus with ARM and A-train observations, *J. Geophys. Res. Atmos.*, 120, 6597-6618.

Um, J., G. McFarquhar, Y. P. Hong, S.-S. Lee, C. H. Jung, R. P. Lawson, Q. Mo, 2015: Dimensions and aspect ratios of natural ice crystals, *Atmos. Chem. Phys*., 15, 3933-3956.

Zhang, K., X. Liu, M. Wang, J.M. Comstock, D.L. Mitchell, S. Mishra, and G.G. Mace, 2013: Evaluating and constraining ice cloud parameterizations in CAM5 using aircraft measurements from the SPARTICUS campaign, *Atmos. Chem. Phys*., **13**, 4963-4982.

Evaluation of 2D-S Data Processing Algorithms

SPEC, Inc. currently uses several different algorithms to derive particle size distributions from individual particle 2D-S images (as described in detail in the appendix of Lawson, 2011). The algorithms to date have been optimized for liquid clouds. Historically, algorithms developed for monochromatic particle imaging probes have not had sufficient resolution to reliably distinguish images with different phase and particle habit. However, with its 10-μm resolution, the 2D-S probe can be used to more reliably distinguish phase and habit. Mixed-phase and ice-only clouds require significant modifications to the conventional algorithms, and this work is ongoing. Three important aspects of ice particles that differ from liquid droplets are: 1) large particle aspect ratios, 2) complex particle shapes, and 3) transmission of light. These three properties of ice particles increase the level of sophistication required

in the data processing algorithms. Below, we first describe the current algorithms and those that were used to process the SPartICus data submitted to the ARM data archive. Discussion of the performance of these algorithms in ice clouds follows. Then, algorithms that were newly developed are described, as well as some of the relevant issues.

The SPartICus, MacPex and TC4 archived 2D-S data were processed using a combination of two algorithms, which will be described briefly below: M4 for particles < 365μm and M1 for particles > 365 μm. Prior to May 2011, the M4 method re-sized out-of-focus images using the Korolev (2007) diffraction correction, then all images were assumed to have a circular cross sectional area and a diameter defined by L4 (see **Figure 1**). This assumption affects the archived data for particles < 365 μm for all of the above projects. The current M4 code (since May 2011) does not assume that all particles < 365 μm are spherical. However, reprocessing with the current code introduces other uncertainties in ice clouds. Comparisons of area distributions derived using different methods are shown and the results are discussed.

M4 Method (after May 2011)

The M4 method uses the length scale L4, which is the maximum particle dimension along the array for a slice of the particle as it transits across the array. An image illustrating the L4 dimension is shown below (from Lawson 2011), where the array is oriented vertically and the particles transit from left to right across the array. Particles that intersect either edge of the array are ignored using the M4 method, since there size cannot be determined.

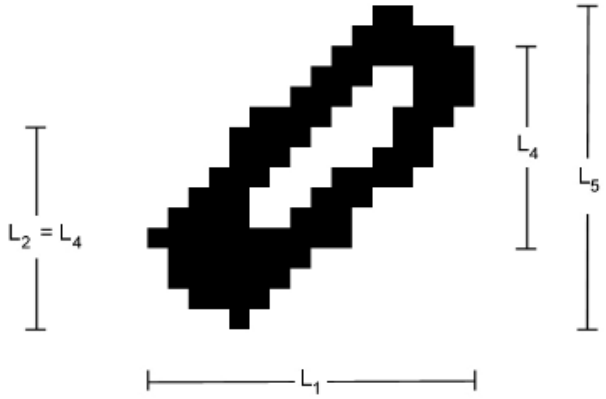

Figure 1. Example 2D-S images demonstrating four measures of image size.

For the M4 algorithms, when the particle image includes > 10% white pixels, it is assumed to be out-of-focus and the size of the particle is corrected according to the ratio of white and black areas (Korolev 2007). This algorithm was designed for correcting the size of spherical particles that are out-of-focus. The particle size after correction is called L7, and L7 ≤ L4. For these particles, the cross sectional area is computed as $\pi(L7)^2/4$.

When the particle is considered in-focus due to < 10% white pixels for that image, the size is not corrected (i.e. L4 is used). In that case, the actual number of black pixels (what we refer to as the "projected area") is used for the particle area unless $\pi(L4)^2/4$ < the projected area. This criterion forces the reported area for that particle to be less than or equal to that of a sphere with the same L4 characteristic dimension. It may be a more appropriate criterion for liquid clouds, where L4 is typically the same as the maximum particle dimension.

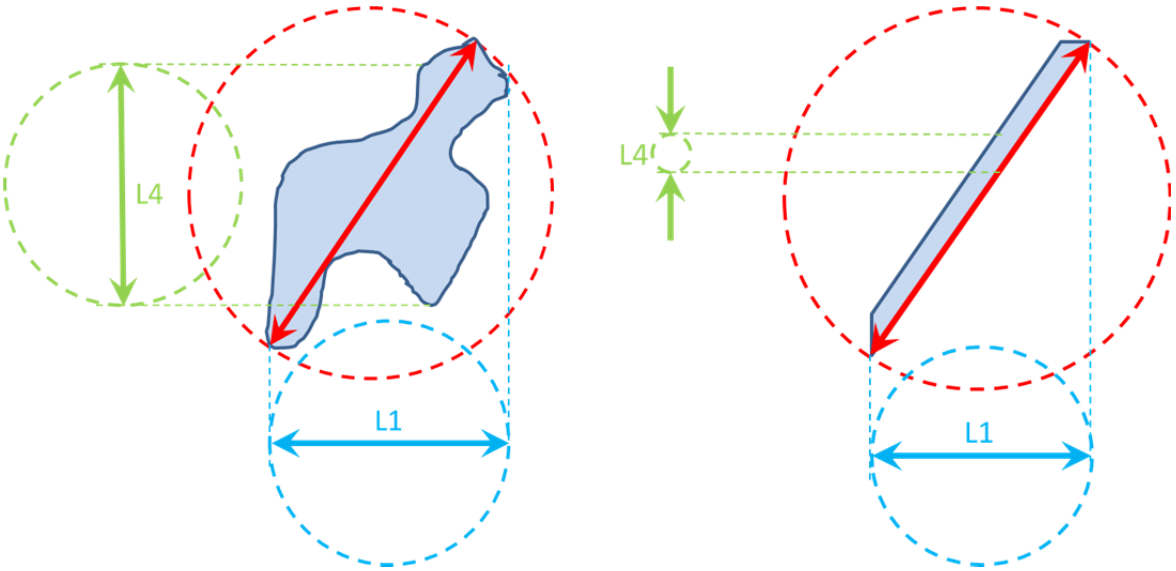

Figure 2. Illustration of particles with aspect ratios > 1, demonstrating differences in L1 and L4 dimensions and corresponding areas.

M4 Method (before May 2011)

The M4 method applied to the SPartICus, MacPex and TC4 datasets was the same as it is now, except that the projected area was never used, and a circular assumption was always made for particles with L4 < 365μm. When the particle was considered out-of-focus due to >10% white pixels, the reported particle area was $\pi(L7)^2/4$. When the particle was considered in-focus, the reported particle area was $\pi(L4)^2/4$.

M2 Method

The M2 method also uses the length scale L4, but the particle size is not corrected for out-of-focus images. The projected area is used for all particles UNLESS $\pi(L4)^2/4$ < the projected area.

M1 Method

The M1 method uses the length scale L1, which is the maximum particle dimension along the direction of travel. The projected area is used for all particles UNLESS $\pi(L1)^2/4$ < the projected area.

Performance of M1, M2 and M4 methods in ice cloud

The L4 and L1 dimensions are not necessarily representative of the maximum dimension of the particle. Depending on aspect ratio and orientation, both L4 and L1 can be significantly smaller than the maximum dimension of the particle. If the L4 or L1 dimension is then used to calculate the particle cross sectional area, then the area can be significantly underestimated as well, as illustrated in **Fig. 2**. The M4 method can be especially problematic in ice clouds because ice particles often have complex shapes resulting in alternating white and black pixels (especially dendrites and aggregates) or they can be semi-

transparent (especially plates and columns), which can cause their images to have a significant fraction of white pixels. Since the M4 algorithm uses the percentage of white pixels to determine if the particle is out-of-focus, this can lead to ice particles being resized, at which point a circular area is applied (reported area = $\pi(L7)^2/4$). A summary of these issues and an example of a projected area distribution from the SPartICus project are shown in **Fig. 3**, with a vertical dashed line indicating the transition between the M1 and M4 methods, where there is a non-physical local minimum.

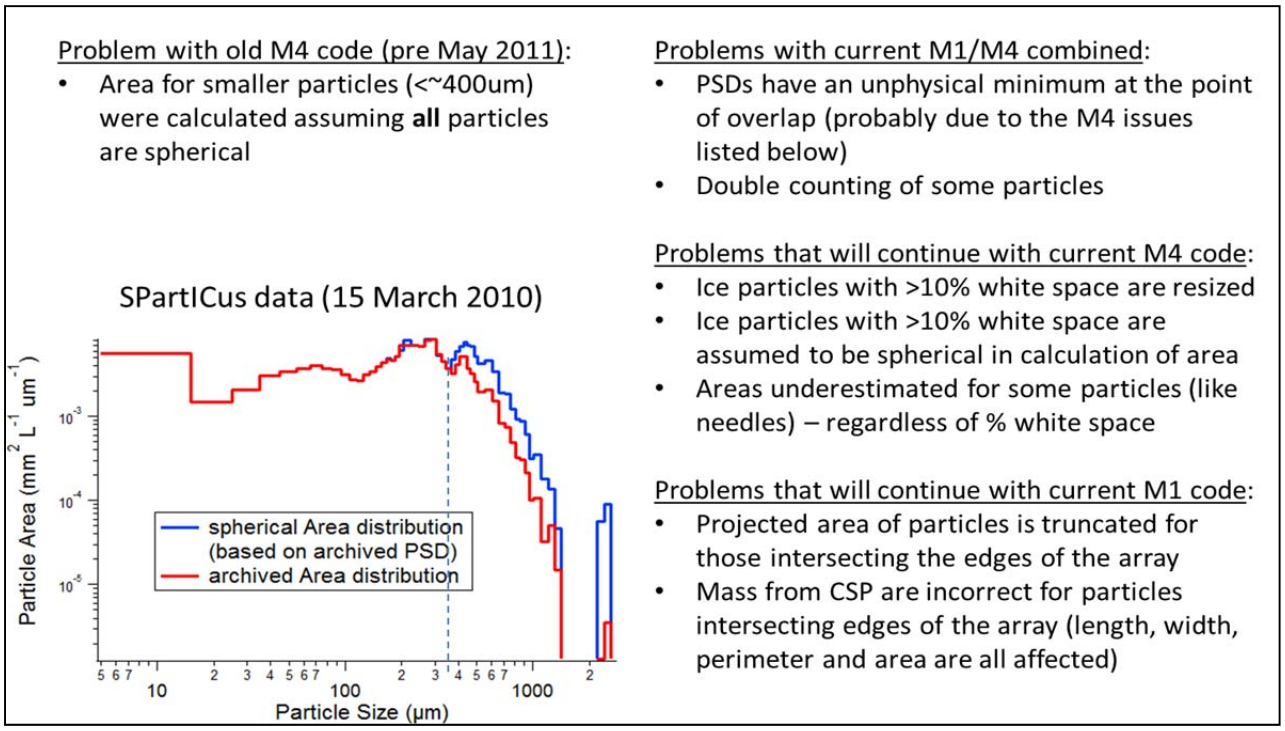

Figure 3. Summary of problems with the previous algorithms.

Figure 4 shows an example of 2D-S observations for a flight in an ice cloud during MacPex, focusing on those particles that are considered out-of-focus by the M4 algorithm. Roughly 40% of particles in the 300-400 µm size range are considered out-of-focus during this time period, and, of these, half are resized by 2 or more size bins using a size correction that is based on spherical particle diffraction.

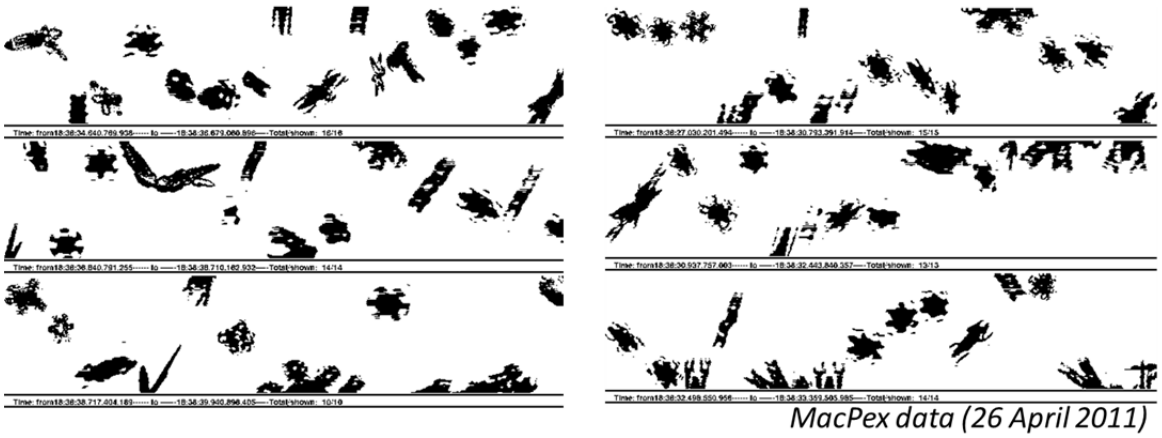

Figure 4. Example 2D-S images of ice particles that are resized by at least two size bins (20 μm) due to the significant fraction of white pixels within each particle image, which the M4 algorithm interprets as the particles being out-of-focus as if they were spheres.

Area Comparisons between Different Algorithms

Several researchers contacted SPEC, Inc. to discuss the archived projected area distributions for the SPartICus dataset, which are important for determining radiative properties of clouds. The main concern was the observed equivalence of the values for area reported for particles < 400 μm with the area for a spherical particle of the same size. To address these concerns, a sensitivity analysis was performed by calculating the area distribution for a given dataset using all available algorithms.

It is not immediately clear which algorithm produced the most accurate results, and it may differ for each case. Dendrites, columns/needles, rosettes and irregular/aggregates are all affected differently by the processing algorithms. Three different time periods (taken from the SPartICus and MacPex datasets) with different ice particle habits were chosen to evaluate potential biases in the area distributions reported in the data archives.

New methods were also created by removing the criterion that limits the reported area to the lesser of the projected area or a circular area with the same characteristic dimension (i.e. $\pi(L)^2/4$). As a result, using these new methods, the reported area for each particle is the projected area. For "donuts", the projected area is the area of the black pixels that make up the perimeter of the image, which can be as much as two times greater than the M4 corrected area (Korolev 2007). The new methods are named "M1 Projected", "M2 Projected" and "M4 Projected", as these new methods are exactly the same as the M1, M2 and M4 methods except that the projected area is always reported, even if the projected area is greater than $\pi(L)^2/4$, where L is L1, L4 or L7, respectively.

Summary of the Archived Data Compared to Other Previously Available Algorithms

Despite the circular assumption used for particles < 365 μm for the MacPex and SPartICus projects, the maximum changes in integrated area for particles 60-365 μm using the currently available methods compared with the archived data is shown to be 3%, 10% and 34% for three test cases shown here. Note that the archived data will be affected the most when the area mean diameter is < 365 μm, or when particles < 365 μm contribute substantially to the total area.

Summary of the Previously Available Algorithms

Current Methods (appropriate mainly for liquid water clouds but also potentially for clouds with dense quasi-spherical particles like hail):

- M1 (all particles including those off the edge of the array, lengthscale perpendicular to array). For use when the TAS is well known and the drop size approaches the size of the diode array FOV.
- M2 (particles all-in, lengthscale parallel to array). Should be using L_5 instead of L_4.
- M4 (particles all-in, lengthscale parallel to array and scaled based on white space). Only appropriate in liquid water clouds or clouds with only quasi-spherical ice. Should also be using L_5 instead of L_4.
- M6 (combination of M2 (sizes < 400um) and M1 (for sizes > 400um), In-focus particles only). For better sizing accuracy and reduced uncertainty in concentrations. Not appropriate for use in clouds with vapor grown ice crystals, low density aggregates or dendrites (because these are not necessarily out-of-focus, but will often be considered as such in this method).

Dendrites/vapor grown crystals (MacPex 2010)

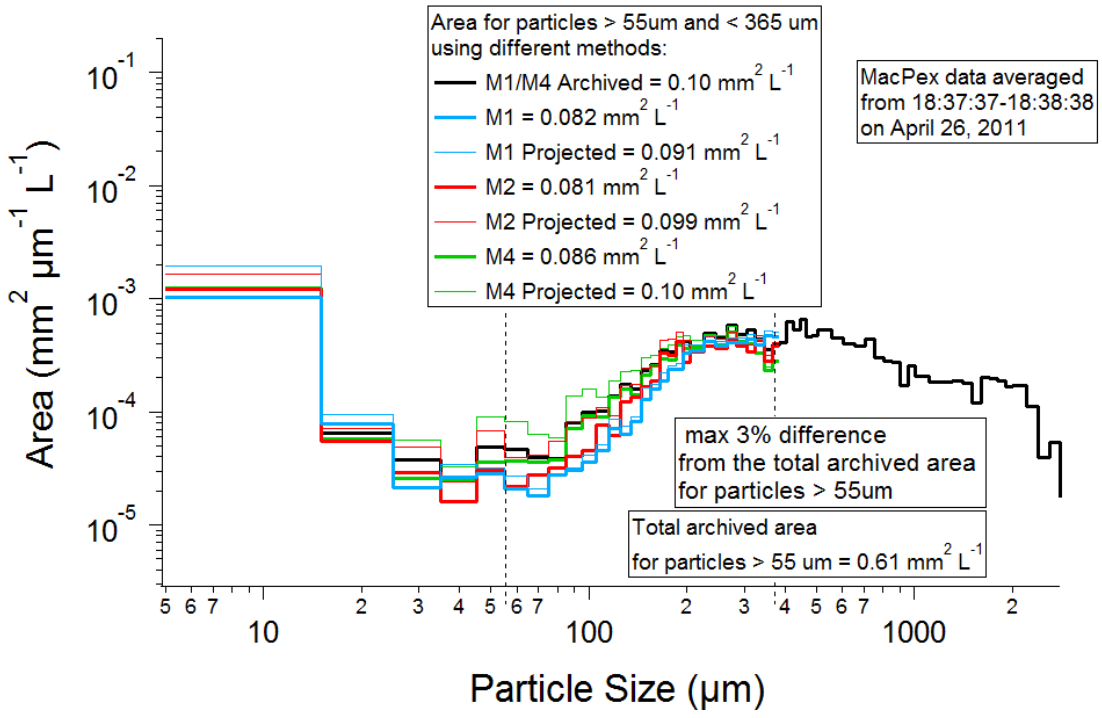

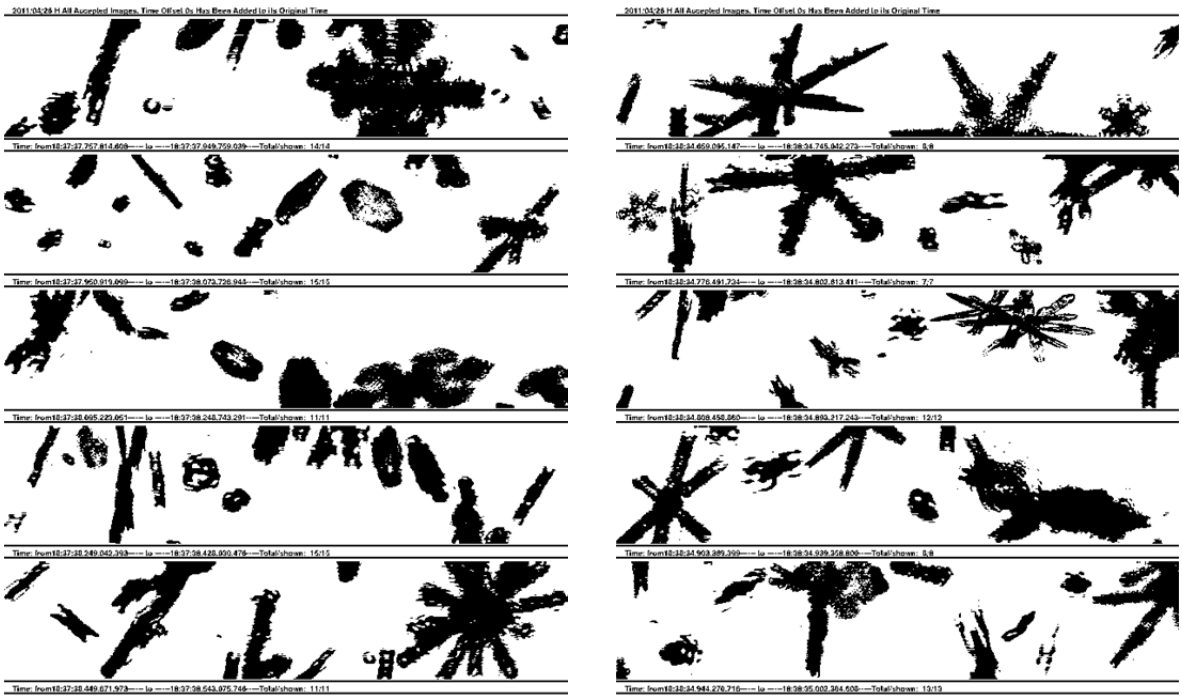

Figure 5. Area distributions using previously available algorithms, with example 2D-S images, for a MacPex example containing a mixture of ice particle habits (mostly vapor grown crystals).

Irregular/Aggregates (MacPex 2010)

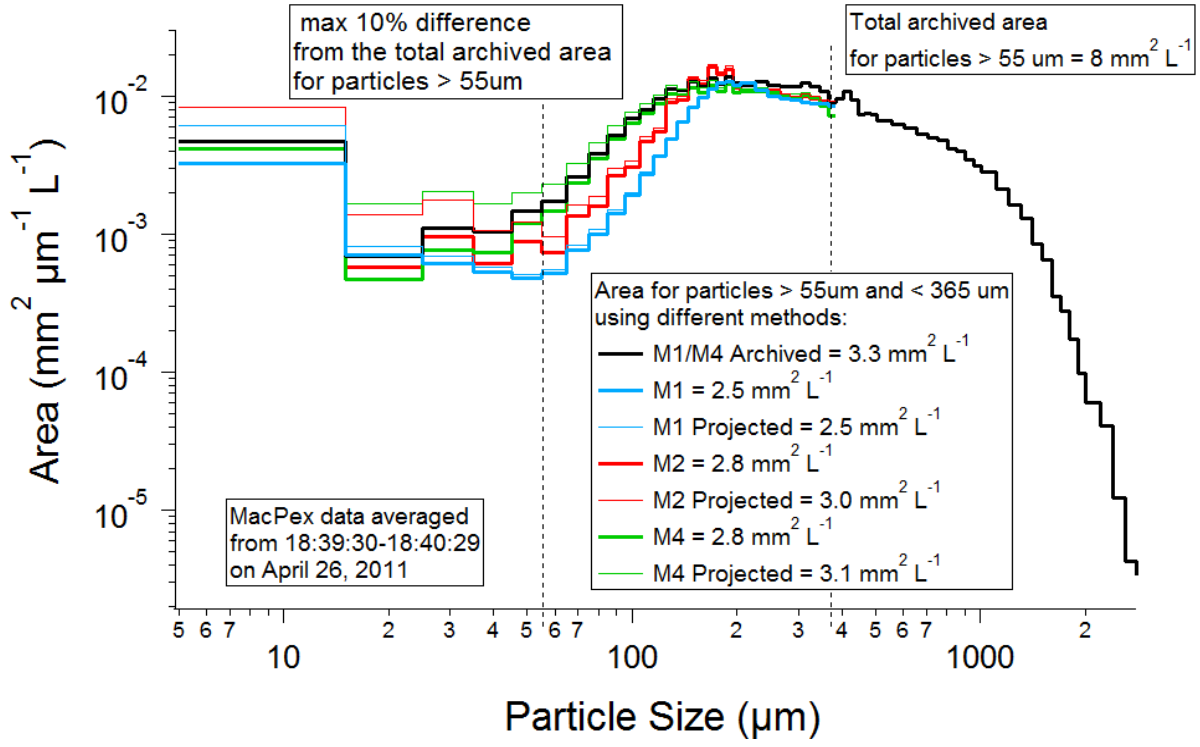

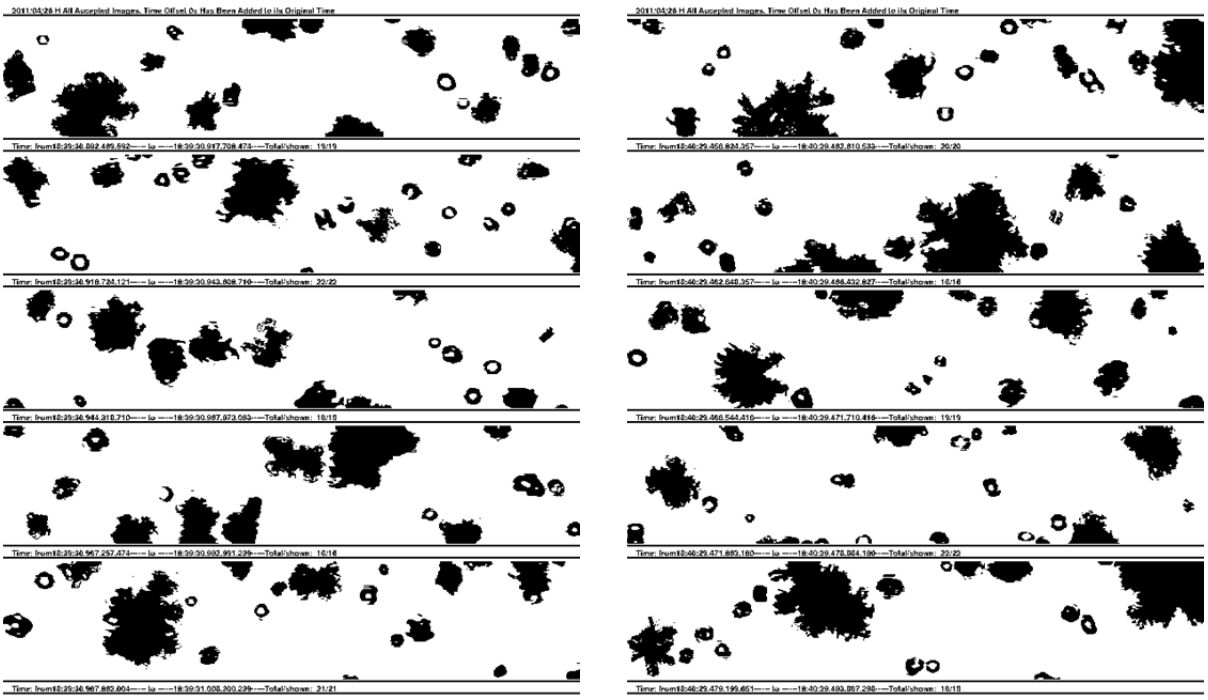

Figure 6. Area distributions using previously available algorithms, with example 2D-S images, for another MacPex example containing low density aggregates and quasi-spherical particles.

Rosettes and small blocky ice (SPartICus 2010)

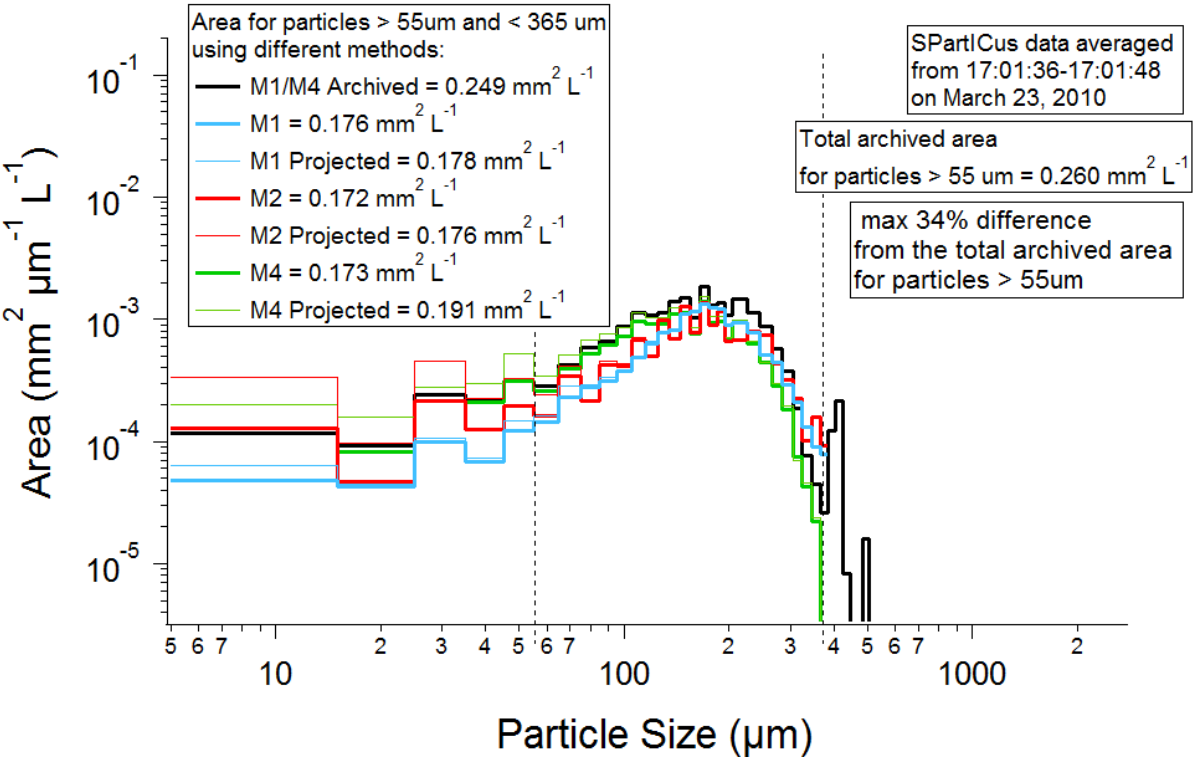

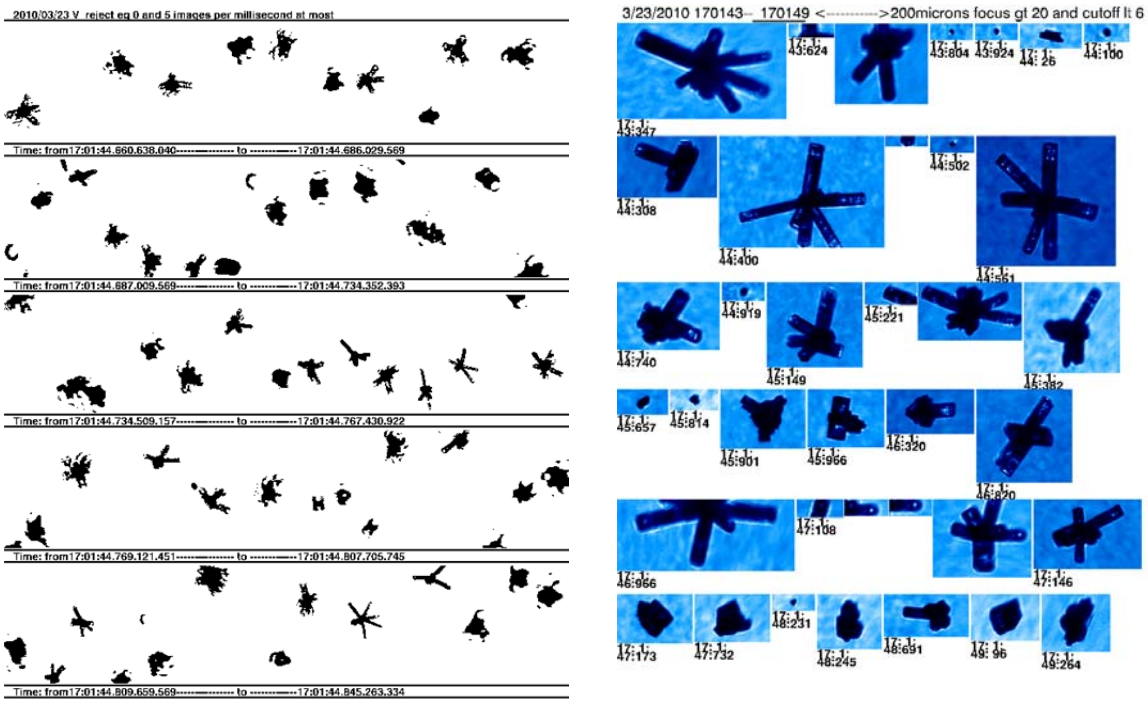

Figure 7. Area distributions using previously available algorithms, with example 2D-S and CPI images, for a SPartICus example containing rosettes and small blocky ice particles.

Development of New 2D-S Algorithms

The main limitation identified for mixed-phase and ice clouds is that out-of-focus spherical particles (whether they are ice or liquid) need to be corrected for diffraction, but the size correction cannot be applied to low-density or semi-transparent ice particles. That means the algorithm must first identify the shape of the particle (round or not) and then only apply the size correction to the spherical particles. Small ice particles often appear to be spherical (Järvinen 2016), therefore the distinction can be important even in ice clouds. Also, the length scales both perpendicular and parallel to the array are insufficient for characterizing the true maximum dimension for ice particles that have large aspect ratios. To address this insufficiency, a new maximum length dimension needed to be quantified.

Furthermore, the mass of ice particles cannot be characterized well with only one particle dimension. In the past, the particle mass has been parameterized based on the measured projected area or the particle maximum dimension. There exist parameterizations for particle mass based on four independent particle parameters: length, width, projected area and perimeter (Baker and Lawson 2006). This 'combined single parameter' estimate of ice particle mass was originally applied to CPI observations, but can now also be applied to 2D-S observations.

Summary of Newly Developed Algorithm

- M7 (particles all-in, max dimension). A New Method similar to M2 (and/or M5), but intended for ice clouds and clouds containing particles with nonspherical particles. This method is significantly different than other methods, because it requires keeping track of sample volume for each particle rather than just based on which size bin the particle falls into (i.e. concentration cannot be simply calculated after accumulating particle counts into size bins), since the probability of including a particle in the analysis depends on the particle orientation and aspect ratio.

More information is now available on a particle by particle basis from the 2D-S observations, such as:

- maximum dimension (neither necessarily perpendicular or parallel to the diode array) this new 'length' is represented by the red arrows in **Fig. 2**
- 'width' – the maximum dimension perpendicular to the particle 'length'
- 'perimeter'
- 'Combined Single Parameter' (CSP), based on 'length', 'width', 'perimeter', and 'area'
- 'mass' based on the CSP parameterization (Baker and Lawson, 2006)
- 'roundness' – described further in the next section

Since 'length' and 'width' are both known, the aspect ratio can now also be reported.

Evaluating Newly Developed M7 Algorithm in Synoptic and Anvil Cirrus

The new algorithm, M7, has a larger effect on particle size and total projected area for anvil cirrus than for synoptic cirrus, as can be seen by contrasting the concentration and extinction comparisons shown in **Figures 8 and 9** for synoptic and anvil cirrus cases, respectively. This is because particles are often 1 mm or larger in anvil cirrus, and are thus more likely to intercept the edge of the 2D-S field of view. Using M1 instead of M7 results in an approximate 5% bias in sample area for synoptic cirrus, and approximately a 13% bias in sample area for Anvil Cirrus.

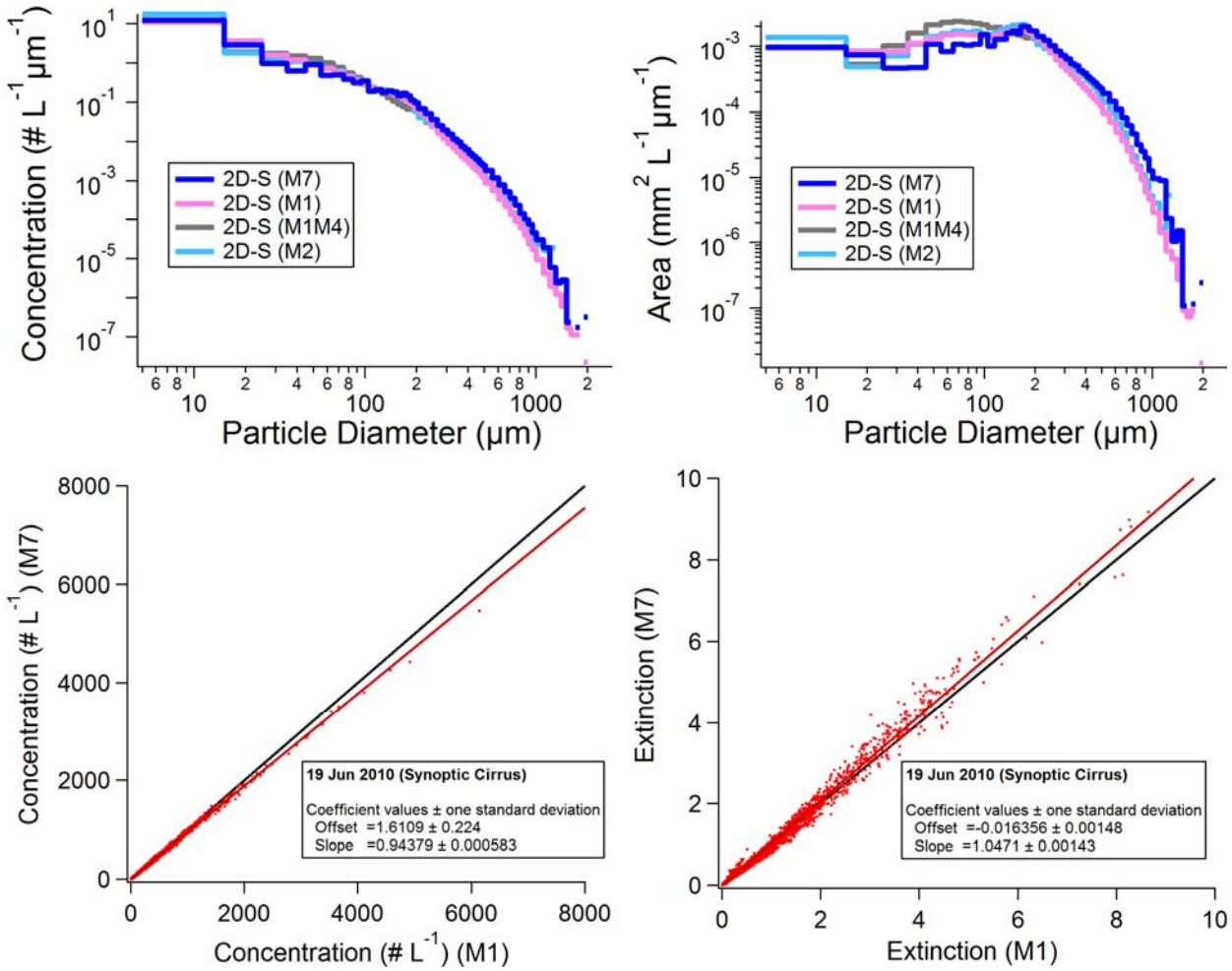

Figure 8. Synoptic cirrus (Top) concentration and area particle size distributions processed using the old (M1, M2, M1M4) and new (M7) methods, and (bottom) comparison of concentration and extinction between M1 and M7.

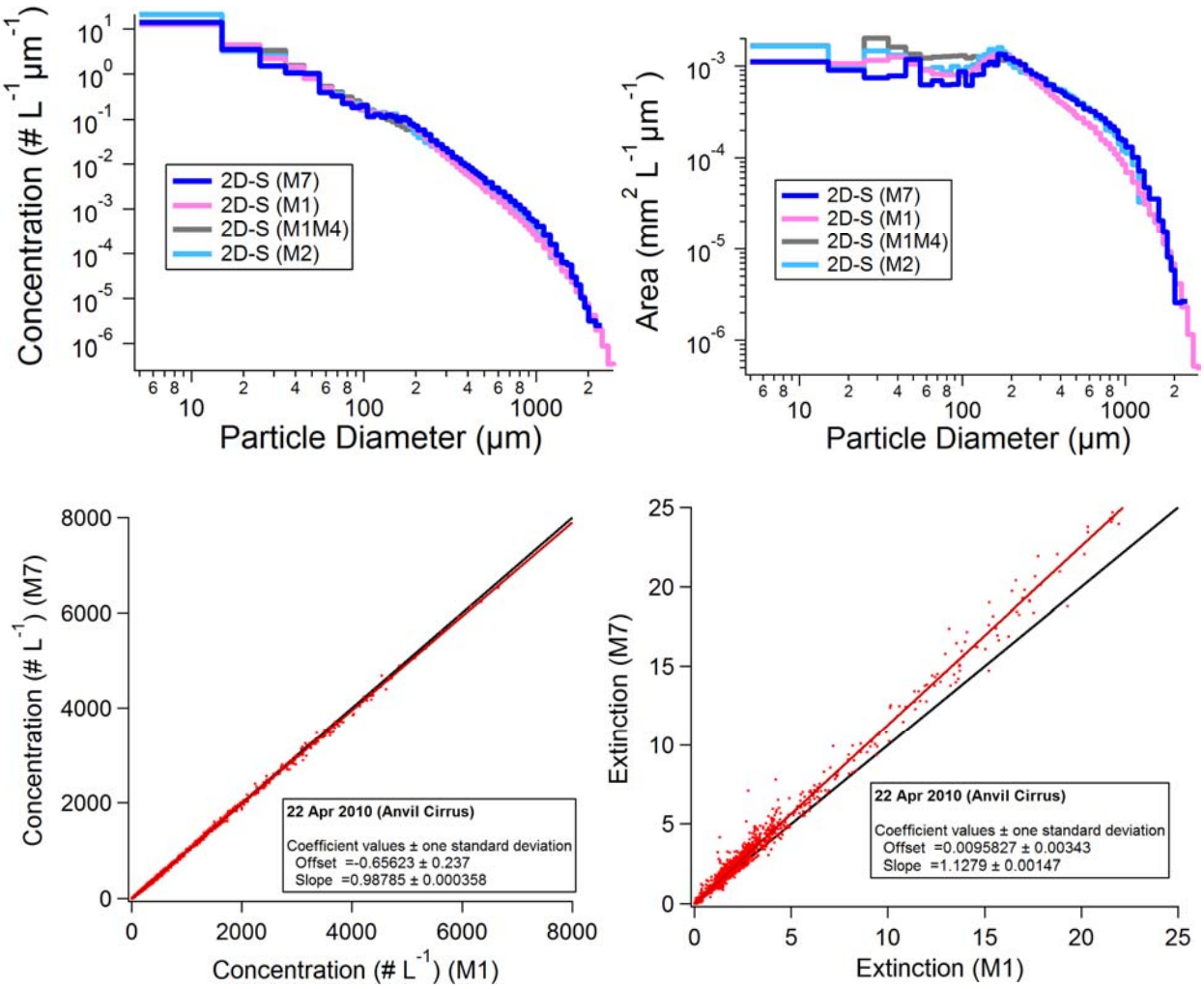

Figure 9. Anvil cirrus (Top) concentration and area particle size distributions processed using the old (M1, M2, M1M4) and new (M7) methods, and (bottom) comparison of concentration and extinction between M1 and M7.

Evaluating Particle Roundness

SPEC, Inc. has incorporated three different measures of particle roundness (as illustrated in **Fig. 10**) into the 2D-S software. These three roundness measures are available for every particle, and can be used to distinguish 'donuts' (out-of-focus spherical images) from ice particles images containing white space.

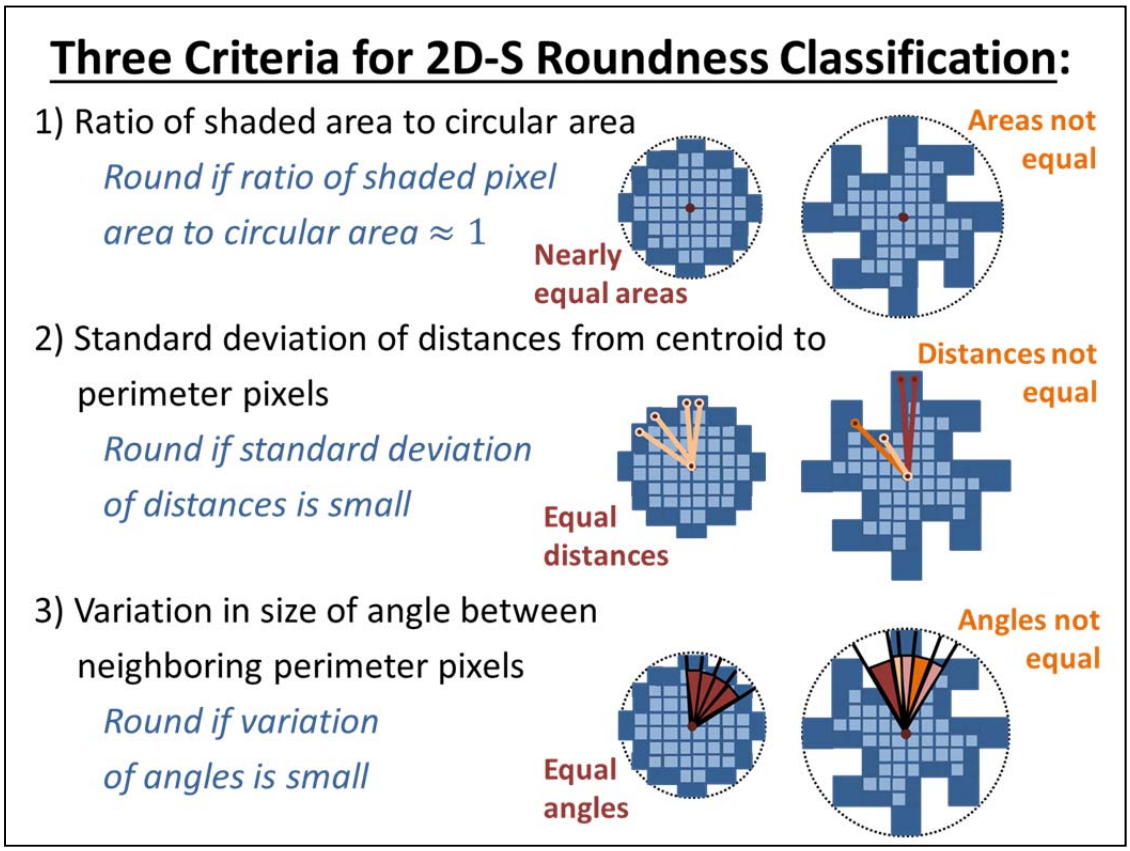

Figure 10. Three independent measures of particle roundness

Figure 11 demonstrates how well the new roundness measures can be applied to distinguish images of ice particles from images of water droplets, in clouds where the ice particles are quasi-spherical (graupel).

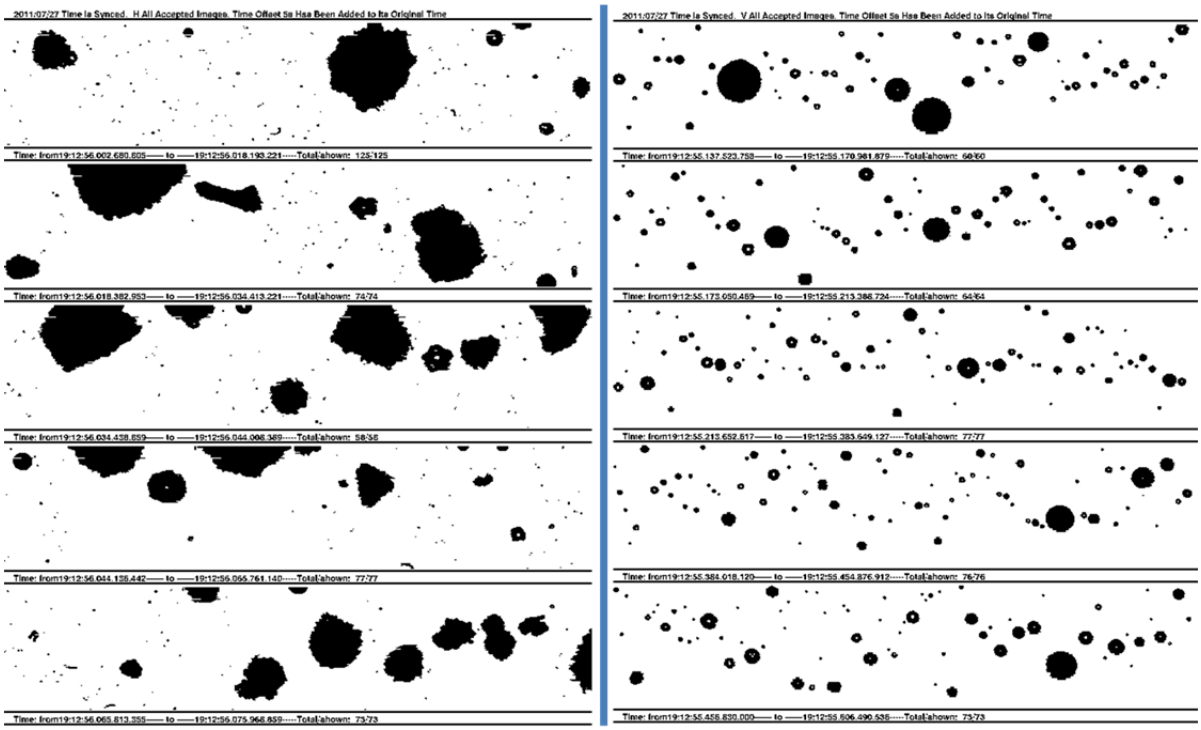

Figure 11. Round (right) and Not-Round (left) particles imaged by the 2D-S for a cloud pass during ICE-T, demonstrating the effectiveness of the new roundness criteria

Calculating Size Distributions from Individual Particle Measurements

Using the newly available particle information, we can determine particle concentrations by first correcting the size of particles that are deemed to be out-of-focus (according to both their roundness measures and percentage of white pixels), and then accumulating particles into the correct size bins. As mentioned previously, the orientation of an aspherical particle affects the probability that the particle will be counted, which means that the sample area varies within a size bin, due to changes in the Effective Array Width (EAW) as a function of both particle size and aspect ratio/orientation (Heymsfield and Parrish, 1978). Consequently, the sample area has to be accumulated on an individual particle basis as well. The 2D-S processing code has been updated and re-structured to allow for this possibility.

Due to their complexity, testing the new algorithms was necessary to evaluate their performance. Simulating known water drop distributions of particle images for input into the 2D-S processing algorithms has been conducted. Laboratory calibration with two-dimensional ice analogues is another way to test the performance of the new algorithms.

Calibration of In-Situ Cloud Probes

Water Droplet Calibration System

To evaluate the diffraction correction for spherical particles and the 2D-S Depth of Field (DoF), a water droplet calibration system initially developed at NOAA (Lance et al, 2010) has been recently duplicated at SPEC, Inc. with minor modifications to accommodate the physical geometry of several different cloud probe instruments. Water droplets are generated at regular intervals using a commercial piezo-electric inkjet device from MicroFab, Inc. The droplets are generated within an evaporation flow tube that uses dry nitrogen sheath flow to control the droplet size and then accelerate the droplets through a nozzle to speeds of up to 20-40 m/s. With the aid of linear translation stages, the droplets are then transmitted at precise positions across the cloud probe sample area to map out the instrument response to water droplets of a known and reproducible size. A microscope with 20x magnification measures the size of the drops as they transit the cloud probe laser beam after exiting the flow tube, providing an independent measure of the droplet size that remains in focus throughout the experiment, which we consider to be the 'true' drop diameter. Since droplets are produced at a controlled rate (e.g. a generation of 100 droplets/second is often used), both the counting and sizing response of the instrument can be tested simultaneously. This is one of the advantages of the water droplet calibrations over the much more commonly performed calibrations using glass beads of known size that are blown haphazardly across the sample area (transiting the sample area at random positions, with random trajectories and at random times), which can thereby only be used to calibrate the average instrument sizing response.

Below is a photograph at 4x magnification of a MicroFab droplet generator as it produces 40 µm droplets at a regular rate of 100 Hz. In this photograph, the droplet generator device was positioned within the evaporation flow tube. The droplets slow down within the evaporation section of the flow tube (which explains the decreased spacing between droplets towards the right in the photograph), but then speed up again when they reach the flow tube nozzle (not shown here). The true orientation of the droplet trajectory is downwards (as in **Fig. 13** and **14**).

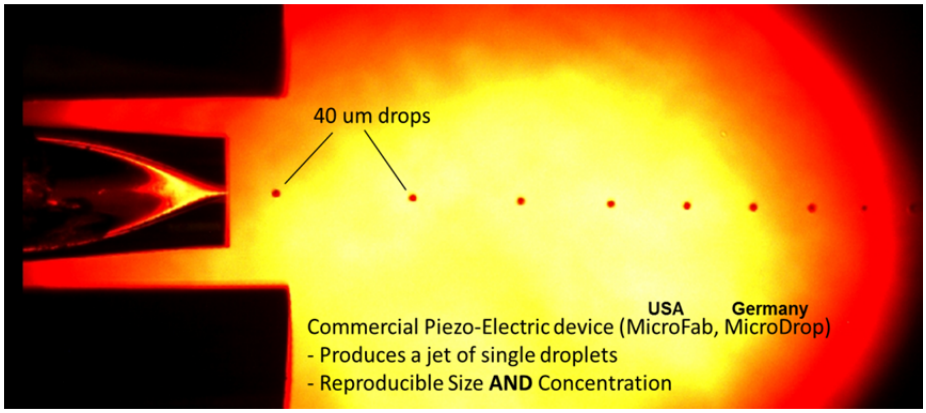

Figure 12. Photograph of 40 µm diameter droplets emanating from a MicroFab droplet generator.

Figure 13 shows a photograph of the droplet calibration system at SPEC, Inc. during calibration of a 2D-128 probe (an instrument equivalent to one channel of a 2D-S probe). 2D-S and FFSSP probes can be calibrated in the same way. The sizing response and sample area of an FSSP and FCDP have also been recently calibrated using the water droplet calibration system at SPEC.

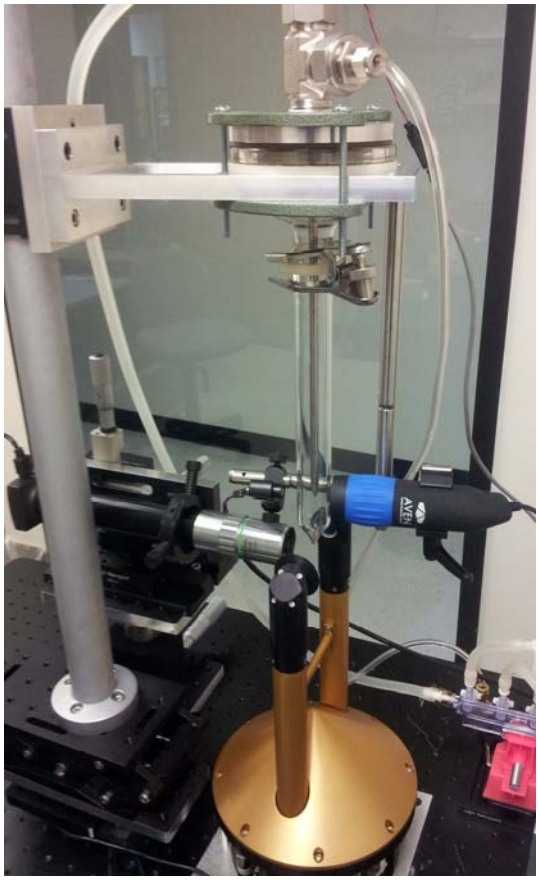

Figure 13: Calibration of a 2D-128 probe.

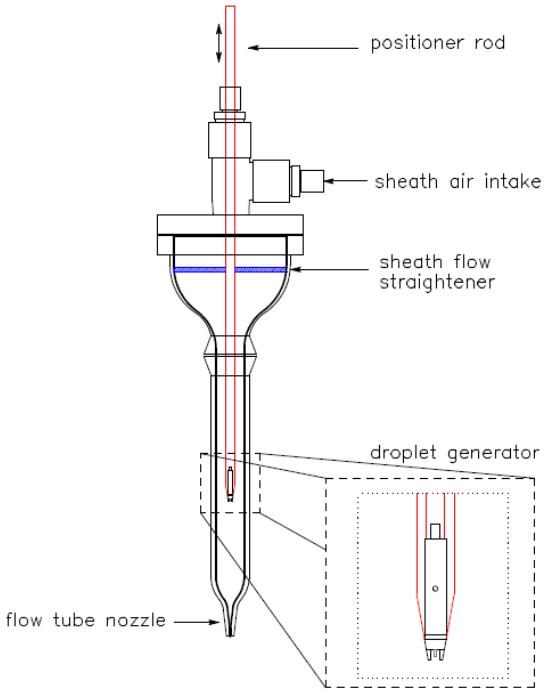

Figure 14: Schematic of the evaporation flow tube.

Calibrating the Sizing Response of the 2D-S with Water Droplets

Below are images of 67 µm diameter droplets acquired by the 2D-128 (**Fig. 15**). The droplet trajectory is from left to right in the figure, and the instrument diode array (128 pixels, with 10 µm spacing) is oriented vertically in the figure. In this example, droplets are positioned near the center of the array and are also centered in the optical depth of the field (DoF), which means the drops are in-focus and are roughly centered between the arms of the 2D-128 (imagine the laser beam going into the page, in **Fig. 15**).

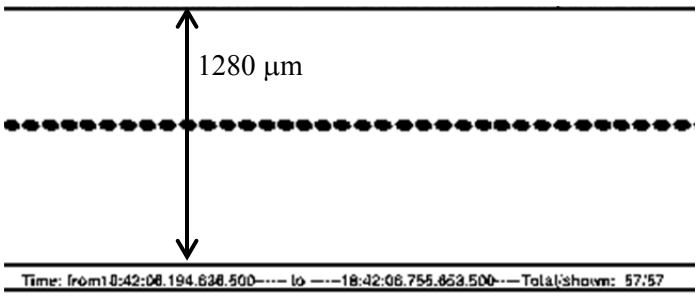

Fig. 15: 67 µm diameter droplets at the center of the Depth of Field (DoF) of the 2D-128 probe.

Fig. 16: Expanded view of droplets shown in **Fig. 15**, demonstrating the reproducibility in both the droplet size and droplet position of the droplet calibration system. Each pixel is roughly 10 µm x 10 µm.

As droplets move away from the center of the DoF (into the page in **Fig. 17**), the drop image increases in size and also develops a white spot at its center, which also increases in size.

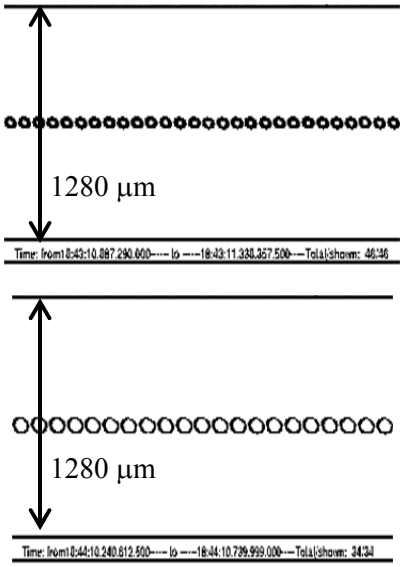

Fig. 17: 67 µm droplets within the DoF of the 2D-128 (4 mm from the center of the DoF).

Fig. 18: 67 µm droplets at the edge of the DoF of the 2D-128 (8 mm from the center of the DoF).

The increase in size of a drop image when droplets are slightly out-of-focus (thereby producing "donuts"), as demonstrated in **Figs. 15-18**, is a fairly well understood optical phenomenon (Korolev, 2007). However, until now there had been no physical validation of the expected performance of the 2D-S with water droplets.

Calibrating the 2D-S Depth of Field (DoF) with Water Droplets

The 2D-S sample area, which is derived from the DoF and effective array width, is important for accurate calculation of drop concentrations. The DoF is strongly dependent on the drop size: DoF = $\pm$ cr^2/λ (Lawson and Cormack 1995), where c is a constant, r is the drop radius and λ is the laser wavelength. Using ray-tracing software, Lawson et al. (2006) determined a value of c = 8 for the 2D-S probe. With the water droplet calibration system, we can now verify the value for 'c' used in the DoF calculation. An investigation using calibrations with 67 µm and 37.8 µm water droplets has produced a value for 'c' that is within 2% and 3%, respectively, of results from the ray-trace determination. This is the first time the DoF has been experimentally verified for a 2D-S probe.

Evaluation of 2D-S Processing Algorithms using Water Droplet Calibrations

We can use the water droplet calibrations to test the 2D-S data processing algorithms, since droplets of known size are transmitted across the 2D-S diode array one at a time at controlled positions. **Figure 19** shows a time series of the 2D-128 calibration with 67 µm diameter water droplets corresponding to the images shown in **Figs. 15-18**. The true droplet size, d_{true}= 67 µm (indicated by the red trace), as measured by a microscope focused on the droplets as they transit along the 2D-128 laser

beam, is constant throughout the entire time series, but the droplet size measured by the 2D-128 (using the M2 method here) grows from ~60 µm to >100 µm as the droplets become more out-of-focus. Near the edge of the DoF, the measured droplet counts decreases until finally the droplets are not detected at all by the 2D-128.

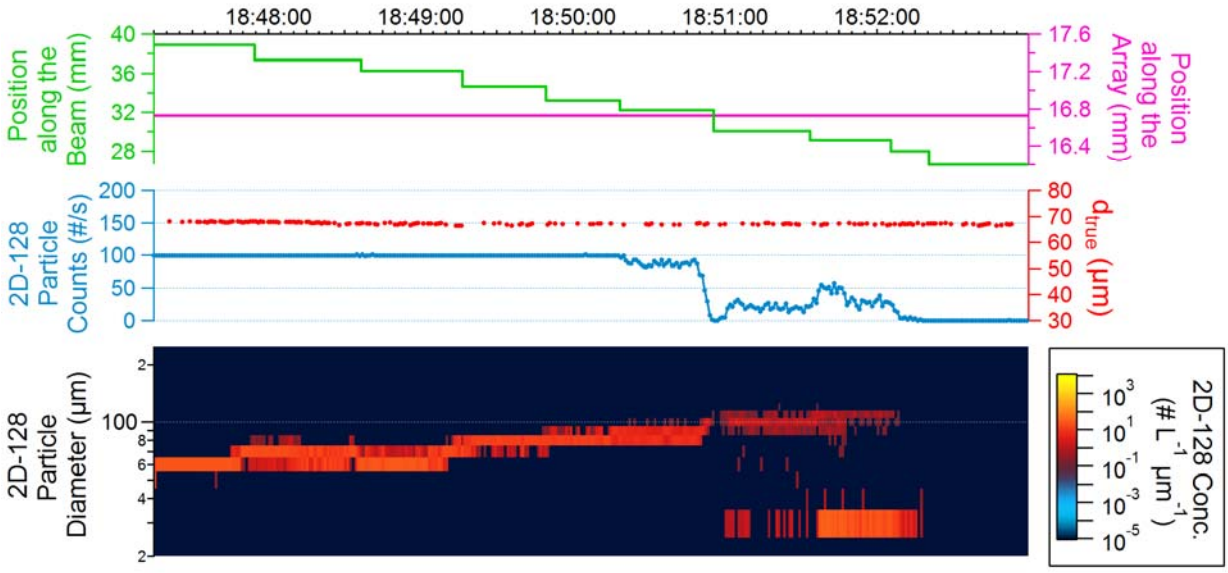

Figure 19. Timeseries of 2D-128 particle size distributions (bottom) and total 2D-128 particle counts (blue trace), as the position of the water droplets (as indicated with the green trace) is moved from the center of the Depth of Field at the beginning of the timeseries to the edge of the DoF until finally the droplets are not detected at all by the 2D-128. Time is indicated at the top of the figure.

The same analysis can be performed using the M1, M4 and M6 algorithms on the same 2D-128 calibration data. Averaging the particle size distributions obtained using all these algorithms over the time period shown in **Fig. 19**, we can see how the measurements respond to droplets of a single size transiting across random positions within the instrument laser beam. **Figure 20** shows the average measured particle counts versus size, while **Fig. 21** shows the average measured particle concentration versus size, using the four algorithms. The 'expected' distribution shown is based on a droplet generation rate of 100/s and the 'expected' concentration is calculated using the measured DoF of 24.4 mm, true air speed setting of 20 m/s and Effective Array Width (EAW) of 1280 µm (since the droplets are all transiting across the center of the linear diode array in this experiment).

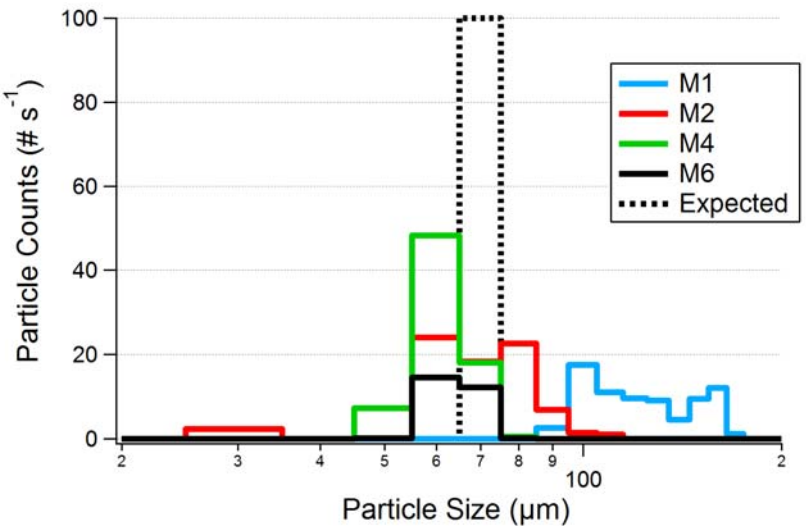

Figure 20. Measured counting response of the 2D-128 to water droplets with 67 ± 0.434 µm (st.dev.) diameter, using the four previously available processing algorithms

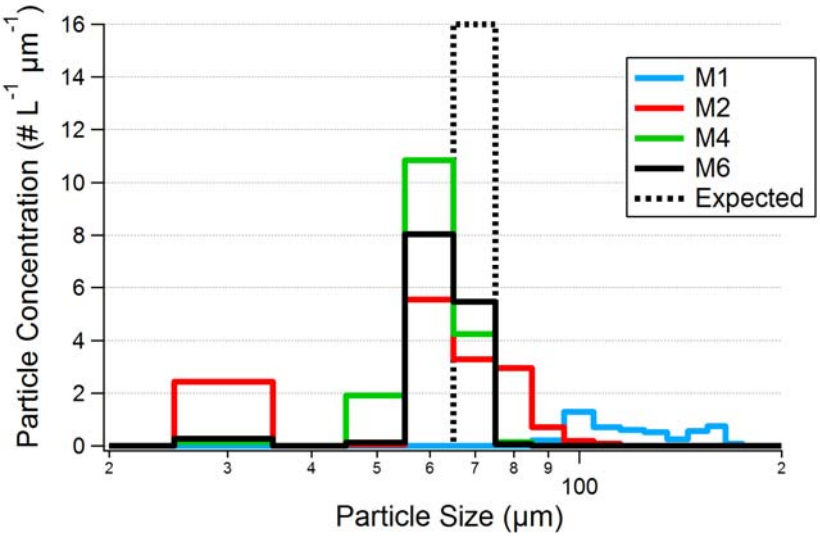

Figure 21. Measured 2D-128 particle size distributions for water droplet calibrations with 67 ± 0.434 µm (st.dev.) diameter, using the four previously available processing algorithms

From **Fig. 21**, we can see that the M6 algorithm, which ignores out-of-focus droplet images, most accurately captures the true droplet size. The M4 algorithm, which includes both in-focus and out-of-focus droplet images and therefore has better counting statistics than the M6 algorithm, also captures the true droplet size to within one size bin. These calibrations demonstrate that the M4 algorithm used for resizing out-of-focus images (based on results from Korolev 2007) works quite well for the 2D-S, although improvements can be made. Both the M1 and M2 algorithms exhibit broad droplet size distributions and over sizing due to out-of-focus droplet images. However, the M1 algorithm over-sizes droplets substantially more than the M2 algorithm due to a true air speed setting that was set too high during the calibration.

In addition to the sizing differences, there are differences in the total concentrations obtained using these different algorithms, because particle concentrations are calculated based on the instrument Depth of Field (DoF), which is strongly dependent on the particle size. Thus, sizing biases result in concentration biases. Although there is a 70% difference in the droplet counting rate between the M4 and M6 algorithms (due to out-of-focus images being ignored in the latter), the concentrations are only 27% different since the DoF for the M6 algorithm is much lower than that for M4. We have experimentally verified the DoF used in the M4 algorithm, but the DoF for in-focus particles used in the M6 algorithm still needs to be verified. Since the droplets are all transiting within the field of view of the 2D-128, across the center of the linear diode array, there is no difference associated with the Effective Array Width (EAW) for each of the algorithms (Heymsfield and Parrish 1978).

These calibration results with water droplets demonstrate that the M6 algorithm is superior to any of the other algorithms in liquid-only clouds (as long as there are sufficient particle counts in the time period of interest). However, the M6 algorithm cannot be used in most ice clouds or mixed-phase clouds since the ice particle images often have complex shapes or are semi-transparent, and the M6 algorithm will inappropriately classify these particles as out-of-focus and ignore them. **Figure. 22** shows a comparison between particle size distributions obtained using the M1 and M6 algorithm in an ice cloud.

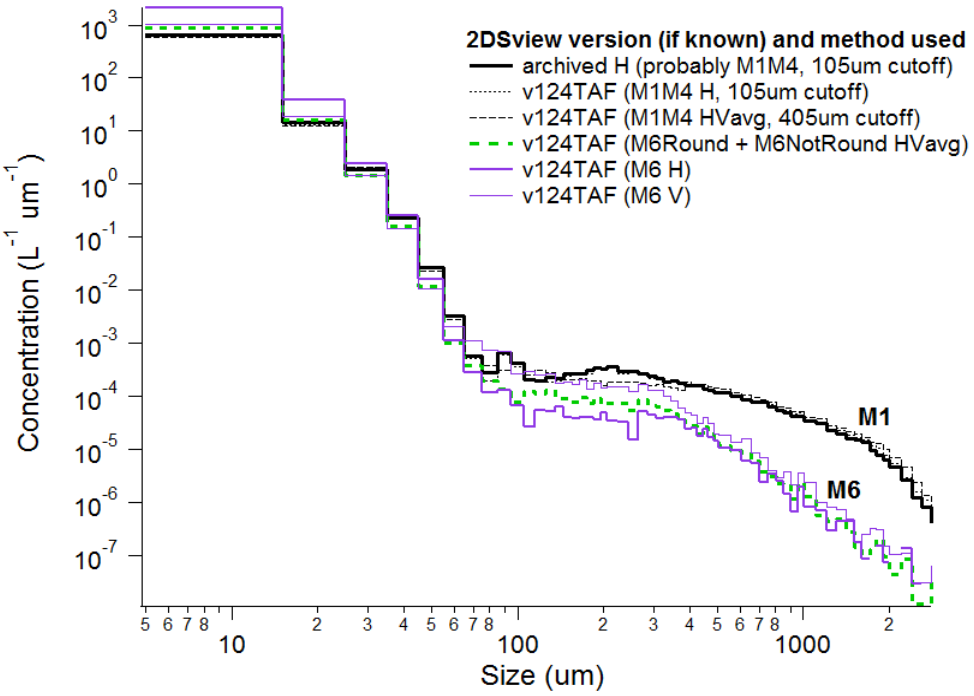

Figure 22. Measured particle size distributions in ice clouds during ISDAC using the M1 and M6 algorithms.

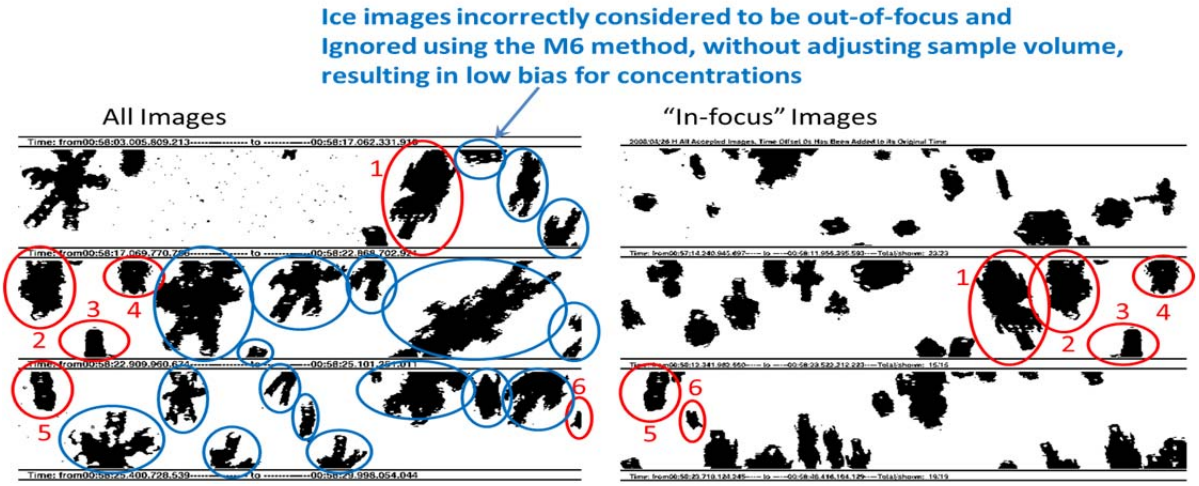

Figure 23. 2D-S Images of dendrite ice particles from the ISDAC 2008 project, showing on the left all images included in the M1 algorithm, and on the right a subset of all images that are considered 'in-focus' (due to <10% of white pixels within the particle area) included in the M6 algorithm.

Figure 23 shows some of the particle images corresponding to the particle size distributions in **Fig. 22** using the M1 (**Fig. 23**, left) and M6 (**Fig. 23**, right) algorithms. The particle images circled in red and numbered in **Fig. 23** are images that are included in both the M1and M6 algorithms; these are particles that are considered in-focus due to < 10% white space within the total particle area. Particles that are considered out-of-focus are circled in blue, and are included in the M1 algorithm but not the M6 algorithm. Here we see that there can be many more particles that are considered out-of-focus than are considered in-focus, and this is especially true for larger particles since the 2D-S images of large dendrites often exhibit alternating black and white pixels.

Calibrating the FCDP Sample Area and Sizing Response with Water Droplets

The FCDP sample area and sizing response was mapped out with a stream of single droplets of known size, by moving the droplet generator incrementally throughout the FCDP laser beam and recording both the qualifier and sizer signals. The maximum qual/sig ratio of ~1 observed at the center of the Depth of Field (DoF) in **Figure 24** (bottom plot) is consistent with the 50/50 beam splitter used. The qualified sample area can be constrained by the criteria that qual > 0.5 * sig.

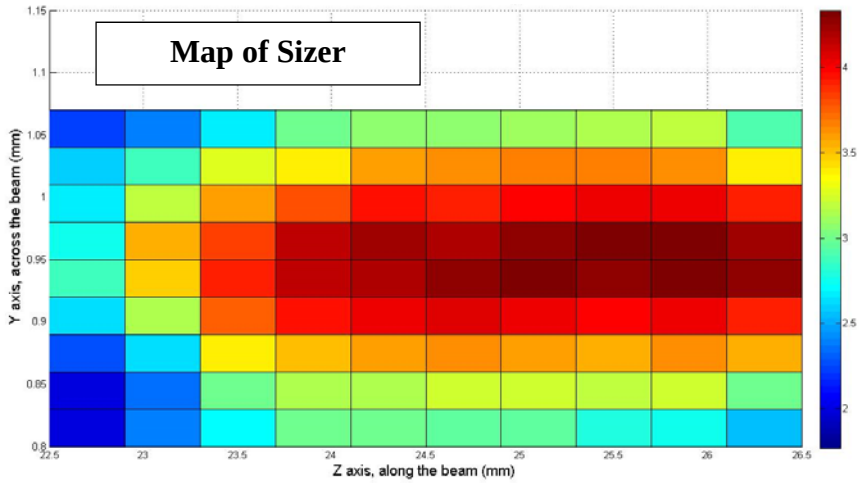

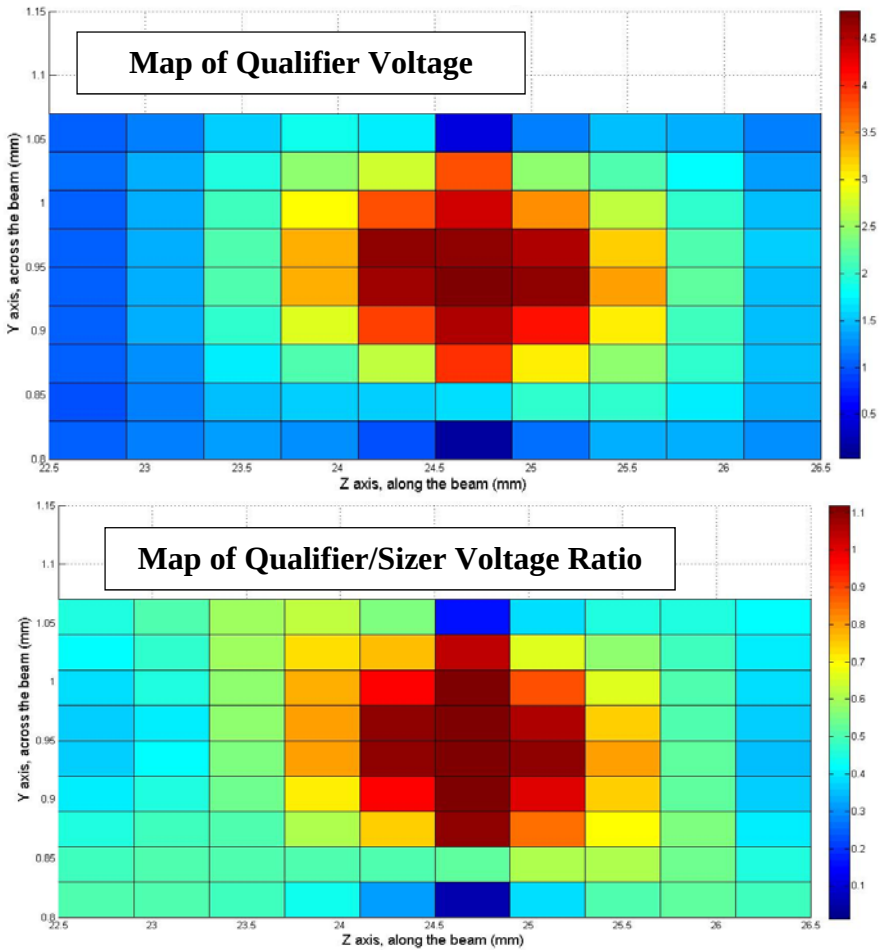

Figure 24: FCDP sample area calibration using water droplets of known size transiting across the FCDP laser beam at known positions.

Analysis of SPartICus Data

Classification of SPartICus Cirrus Ice Particle Habits within Different Temperature Regimes

Ice particle habits were identified with an auto-classification scheme and also verified visually. **Figure 25** shows example images from the auto-classification scheme used to quantify ice particles with a maximum length larger than 50 µm into 6 distinct habit categories: Spheres, Columns, Plates, Rosettes, Budding Rosettes and Irregular particles. It is rather difficult to clearly assess the shape of CPI particles smaller than 50 µm in diameter. Although not shown, most aggregate particles fall into the Irregular category. The classification of synoptic cirrus into different temperature regimes (205-215 K, 215-225 K, and 225-235 K) did not yield obvious differences with regard to ice particle habit. The time periods of interest representing synoptic cirrus within each temperature regime were provided by Eric Jensen and coincide with his analysis of ice particle concentrations reported in the SPartICus 2012 Annual Report. All habit types (rosettes, columns, plates, aggregates) were found in all temperature regimes CPI synoptic cirrus images from the different temperature regimes are shown in **Fig. 26**. These images are a small sample of all images in each temperature category and were manually chosen to represent the range and approximate proportions of habit types observed. The actual percentages of the various habits that were

observed in each temperature region, separated by number, area and mass, are shown in **Fig. 27**. The biggest visually apparent difference in the CPI images between each temperature regime was an increase in the particle size at warmer temperatures.

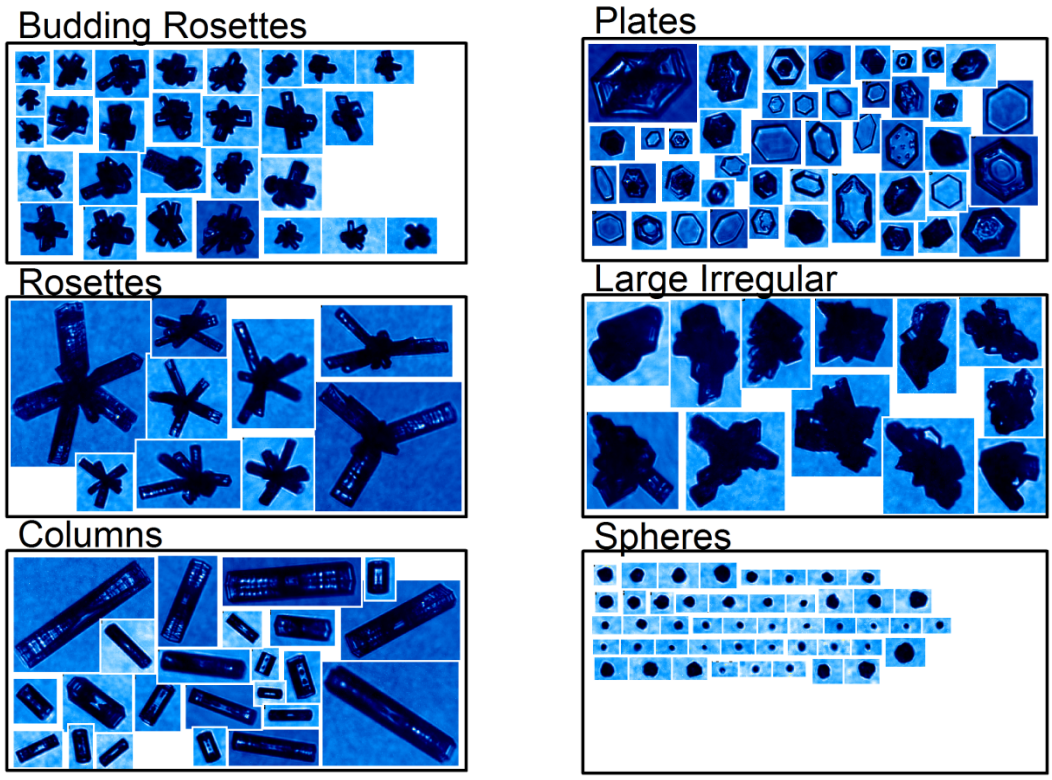

Figure 25. Auto-classification scheme used to distinguish ice particle habit from CPI images.

Temperature Regime 1 (205-215 K):

Temperature Regime 2 (215-225 K):

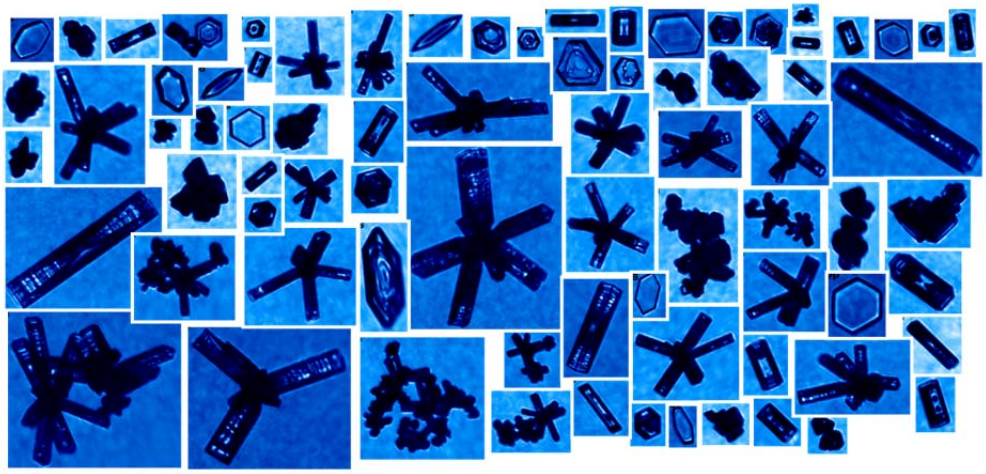

Temperature Regime 3 (225-235 K):

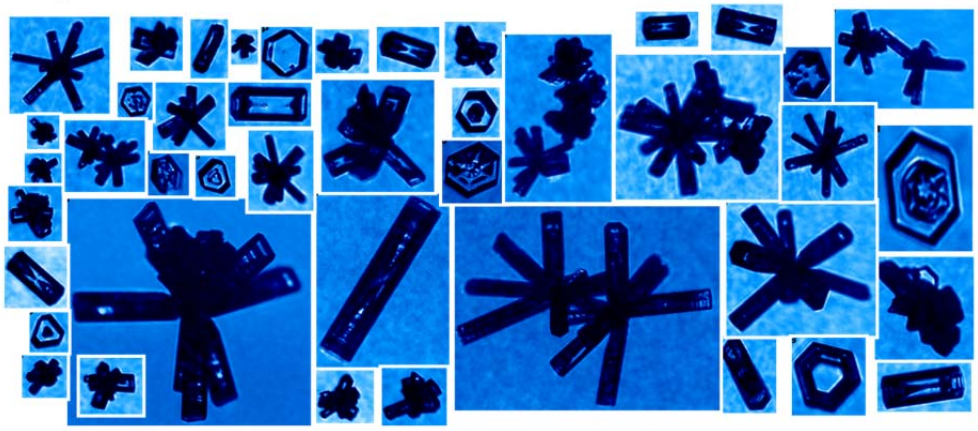

Figure 26. Representative synoptic cirrus ice particle images obtained with the CPI for the different temperature regimes during SPartICus.

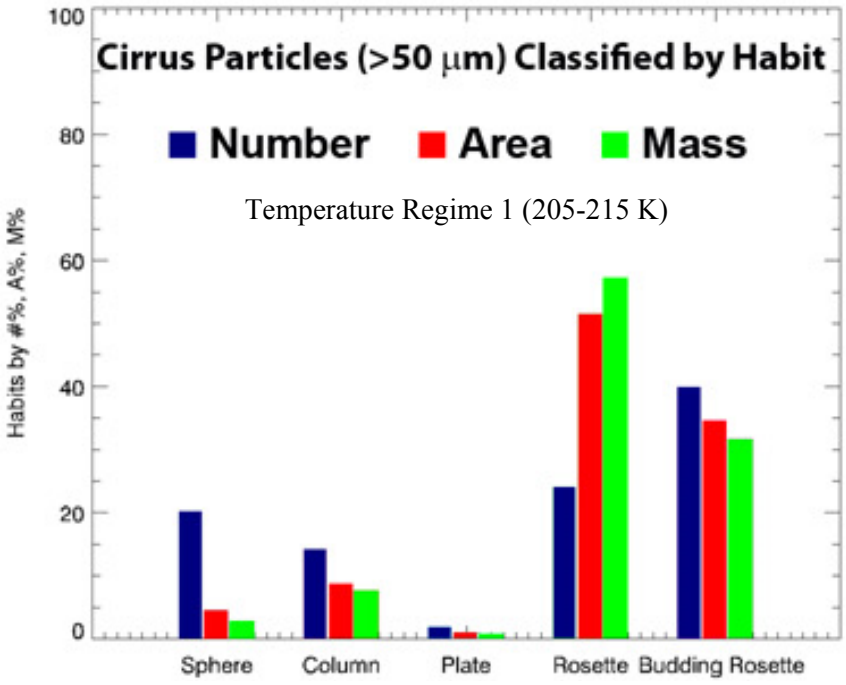

Temperature Regime 1 (205-215 K)

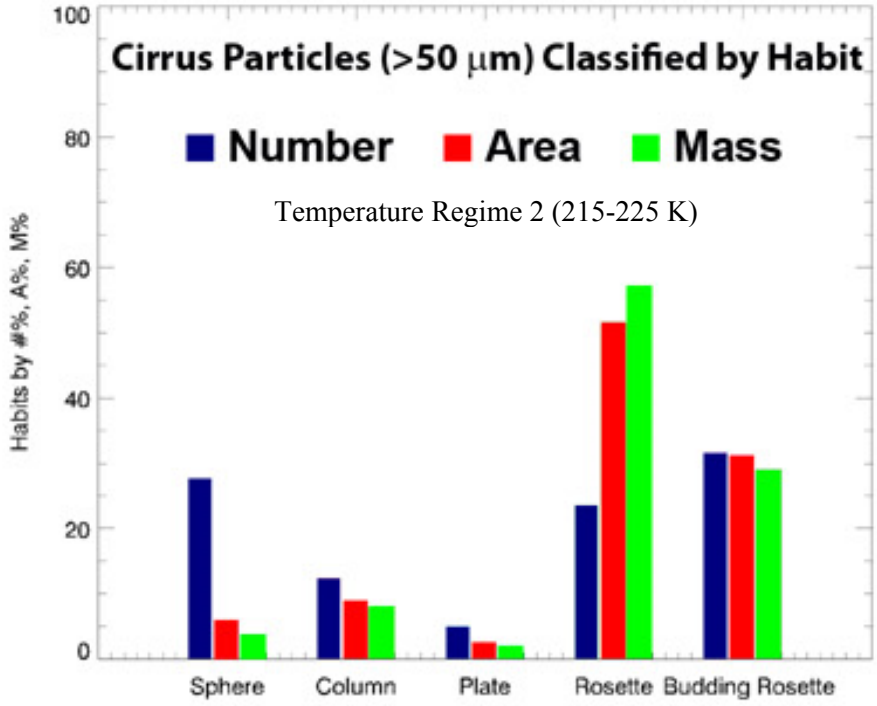

Temperature Regime 2 (215-225 K)

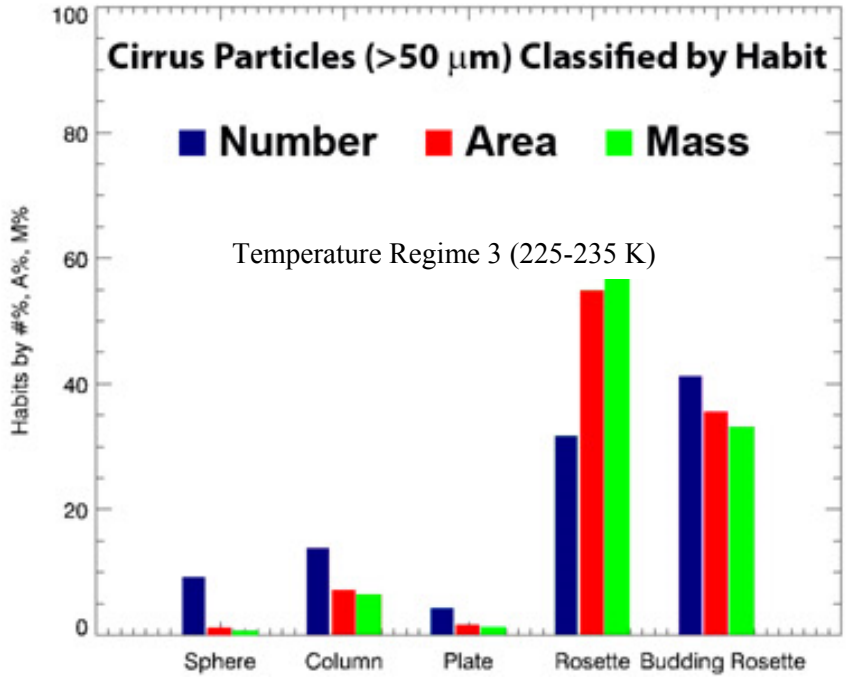

Figure 27. SPartICus ice particle habits as number, area, and mass percentages corresponding to the CPI representative synoptic cirrus images and temperature regimes shown in **Figure 26.**

In addition to computing the particle counts corresponding to different habits, the auto-classification scheme also records each particle's maximum dimension. This allows for a particle size distribution to be obtained corresponding to the different particle habits, as shown in **Fig. 28** for the three different temperature regimes. This is accomplished by first calculating the fraction of particle counts within a given size bin and with a given habit classification using the CPI images, and then multiplying this fraction by the total particle concentration measured by the 2D-S for the same size bin. The high resolution grey-scale CPI images are used to determine the particle habit, while the 2D-S measurements are used to quantify the particle concentration, and both are used together to derive particle size distributions for the different habits. This method assumes that there are no habit-dependent biases in particle sampling within the CPI for particles with the same maximum dimension.

The results with auto-classification demonstrate what is visually apparent from the CPI images, 1) spherical particles are generally small (< 200 μm), columns span a wide range of sizes (20-1000 μm), budding rosettes have a modal diameter of 100-300 μm, the majority of the largest particles observed are rosettes, and the size of vapor grown particles like columns, plates and rosettes increase with temperature. The "Total" size distributions shown in **Fig. 28** are directly from the 2D-S observations, averaged for each temperature regime.

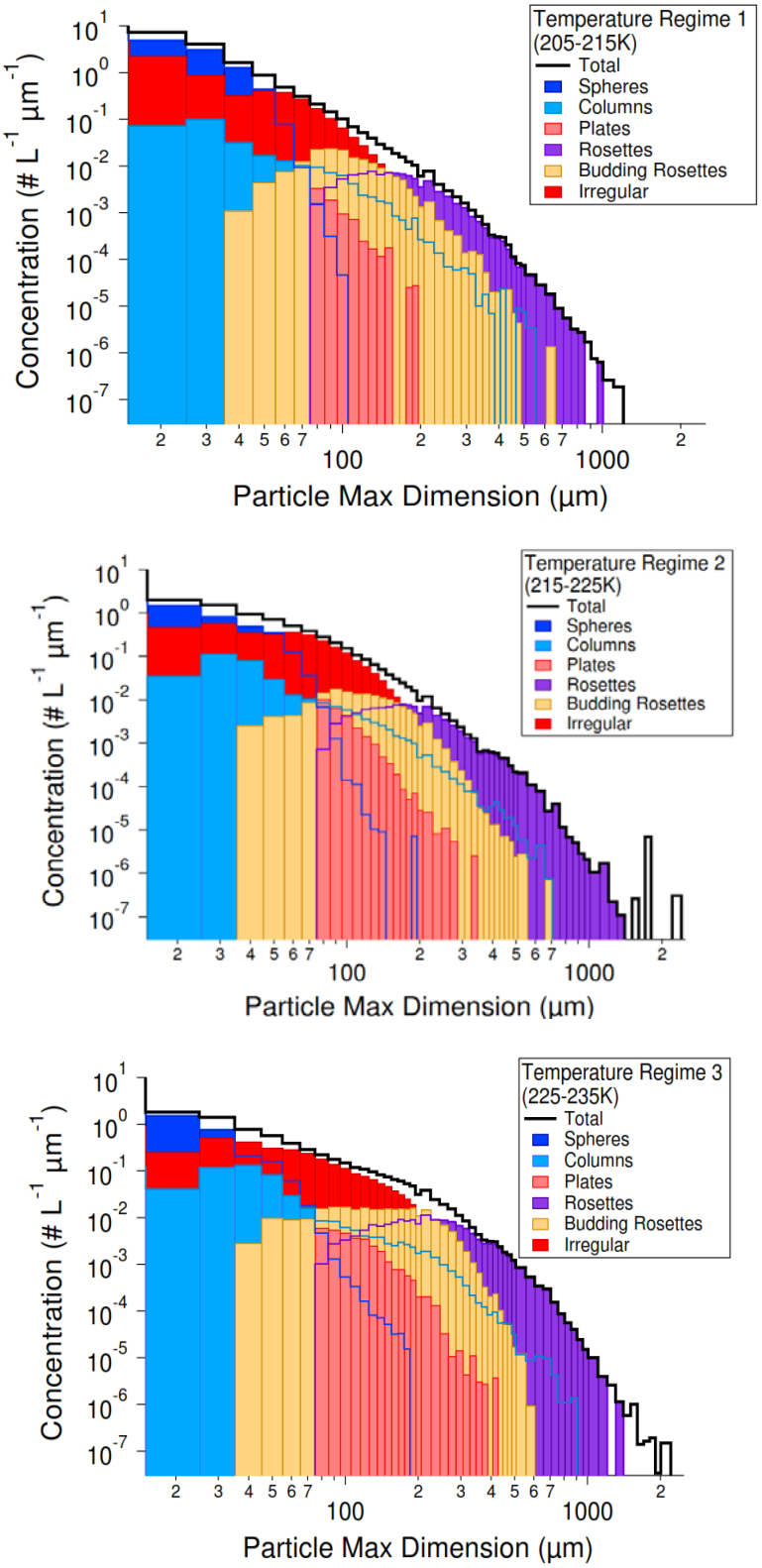

Figure 28. Particle size distributions classified by habit, for the three temperature regimes.

Classification of SPartICus Cirrus Ice Particle Habits According to Atmospheric State

The number of particles within each habit category are not significantly different between the three different temperature regimes. More distinct than the change in particle habit with temperature is the change in particle habit with different atmospheric states, or weather patterns. Muhlbauer et al. (2014) characterized the atmospheric state for the SPartICus project and identified three persistent features typical of synoptic cirrus in the vicinity of the ARM SGP site, which are described as: 1) Ridge Crest, 2) SubTropical Jet, and 3) Frontal Cirrus. According to Muhlbauer et al. (2013), the Ridge Crest atmospheric state represents a large amplitude ridge with anticyclonic flows over North America and a high pressure system with ridge axis approximately centered at the ARM SGP site, the SubTropical Jet atmospheric state represents an approaching deep trough with embedded Jetstream and southwesterly flows leading to advection of moist subtropical air towards the ARM SGP site, and the Frontal atmospheric state represents a deep upper-level trough and low pressure system with embedded cold front, south-westerly flows at the ARM SGP site and a Jetstream pattern slightly east of the ARM SGP site.

The CPI images obtained within synoptic cirrus for flight days classified according to these three different atmospheric states showed distinct particle habits. **Figures 29 - 32** show representative CPI images for these three synoptic cirrus cloud types as well as Anvil cirrus. The corresponding flight days and description of the dominant ice particle habit are given in the table below.

Atmospheric State	Flight Dates	Dominant Habit
Ridge Crest	Mar 19, 30, Apr 1, 28, 29	Rosettes
SubTropical Jet	Jan 14, 15, 31, Feb 1, 3, 4	Columns/Plates/Sideplane Rosettes
Frontal	Jan 19, 20, Mar 27	Aggregates/Rosettes
Anvil	Jan 21, Jun 14, 15, 23	Large complex aggregates/ Sublimated

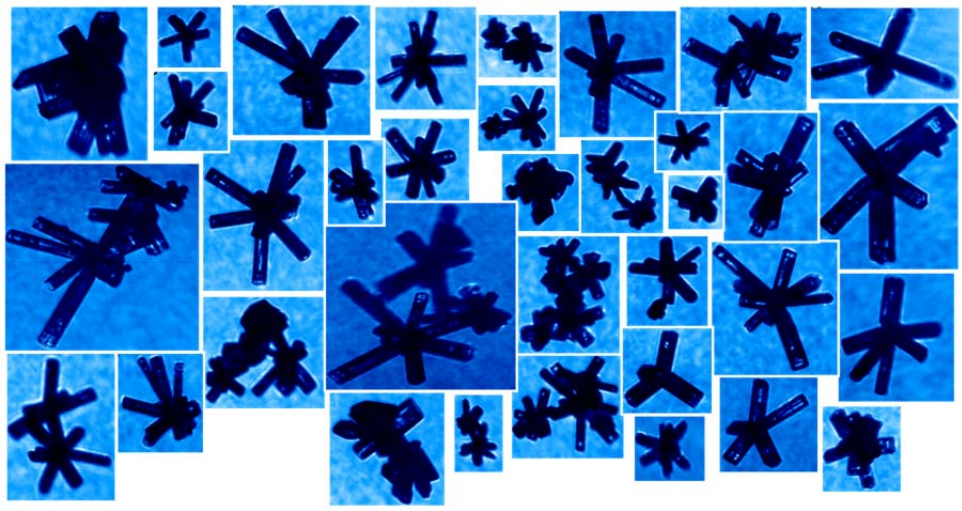

Figure 29. CPI images obtained in cirrus corresponding to the Ridge Crest atmospheric state

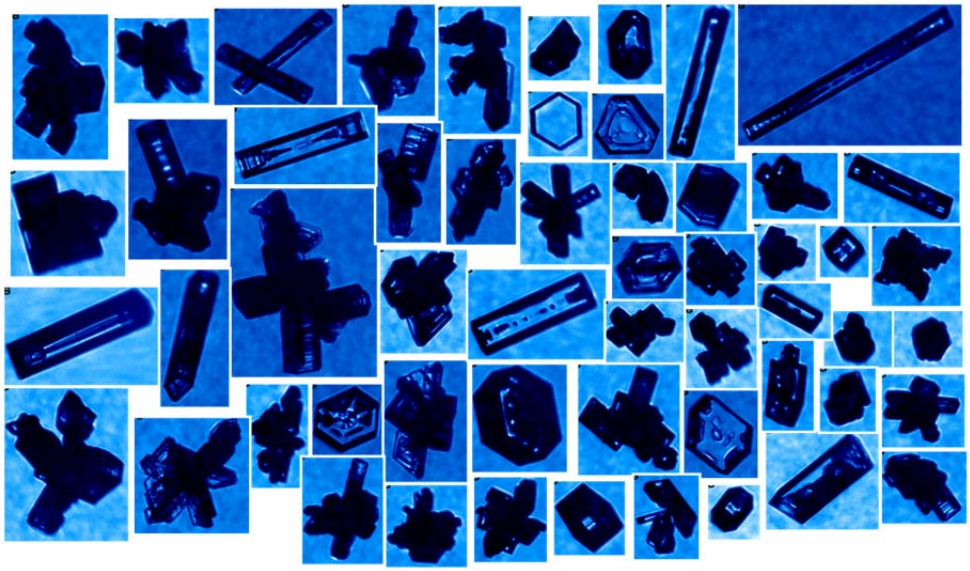

Figure 30. CPI images obtained in cirrus corresponding to the SubTropical Jet atmospheric state

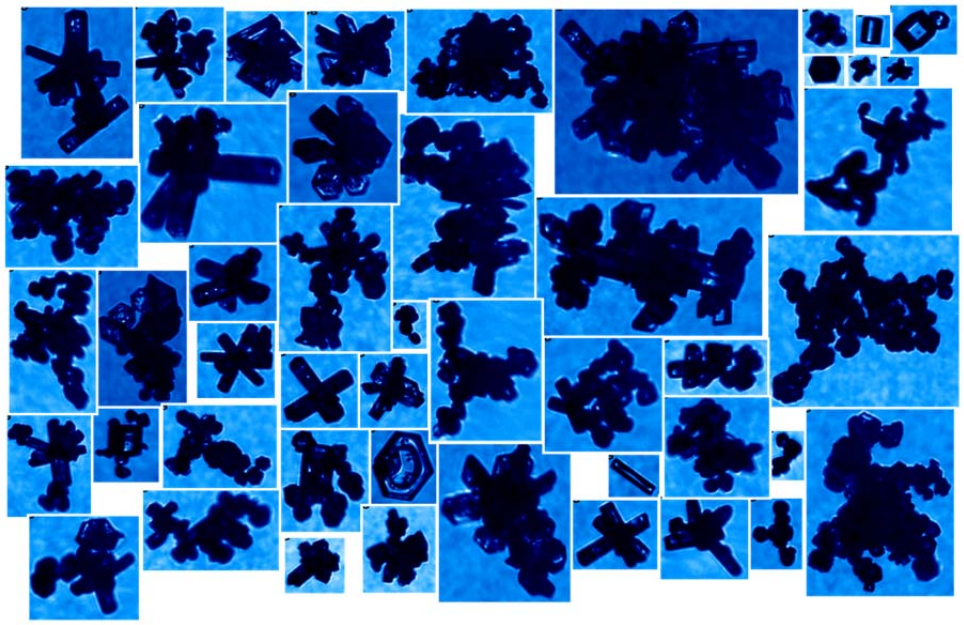

Figure 31. CPI images obtained in cirrus corresponding to the Frontal atmospheric state

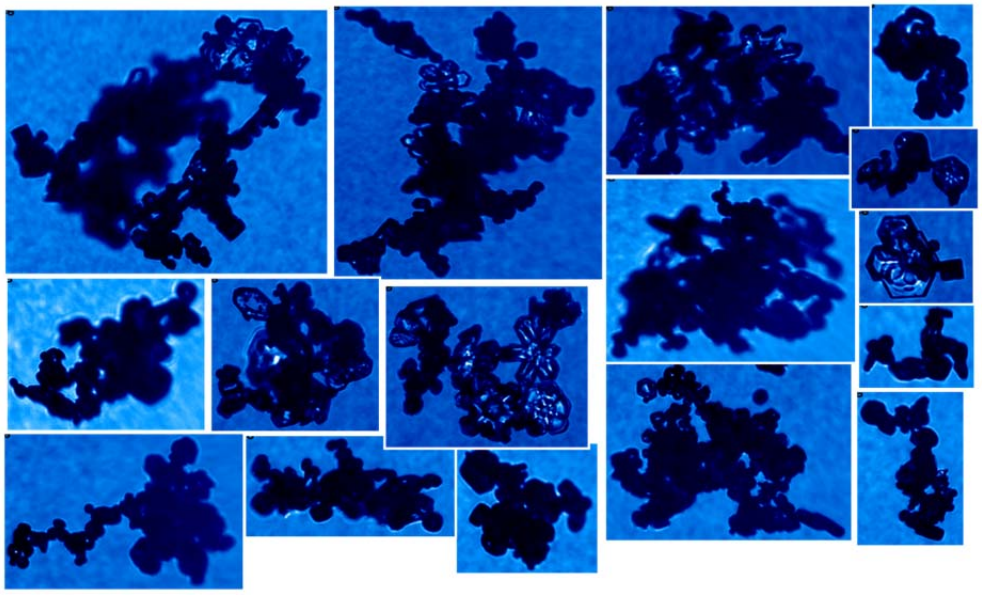

Figure 32. CPI images obtained within Anvil Cirrus

Mass-Dimension Area-Dimension Reprocessing

Special reprocessing of the SPartICus Lear in situ data was performed to assist with analysis of mass-dimension and area-dimension parameterizations (Erfani and Mitchell 2015). For this analysis, the 2D-S data was reprocessed to include computation of the area ratio and width-length ratio in each bin. These data were then combined with CPI data, separated into temperature regions, and fit with second order polynomials to extract m-D and A-D relationships for each temperature region. The plots in **Figures 33** and **34**, from Erfani and Mitchell (2015), show the A-D and m-D power law fits, respectively, to the in situ data. These new m-D and A-D fits to the in situ data improve confidence in remote sensing retrievals of cloud properties and cloud radiative properties in climate models.

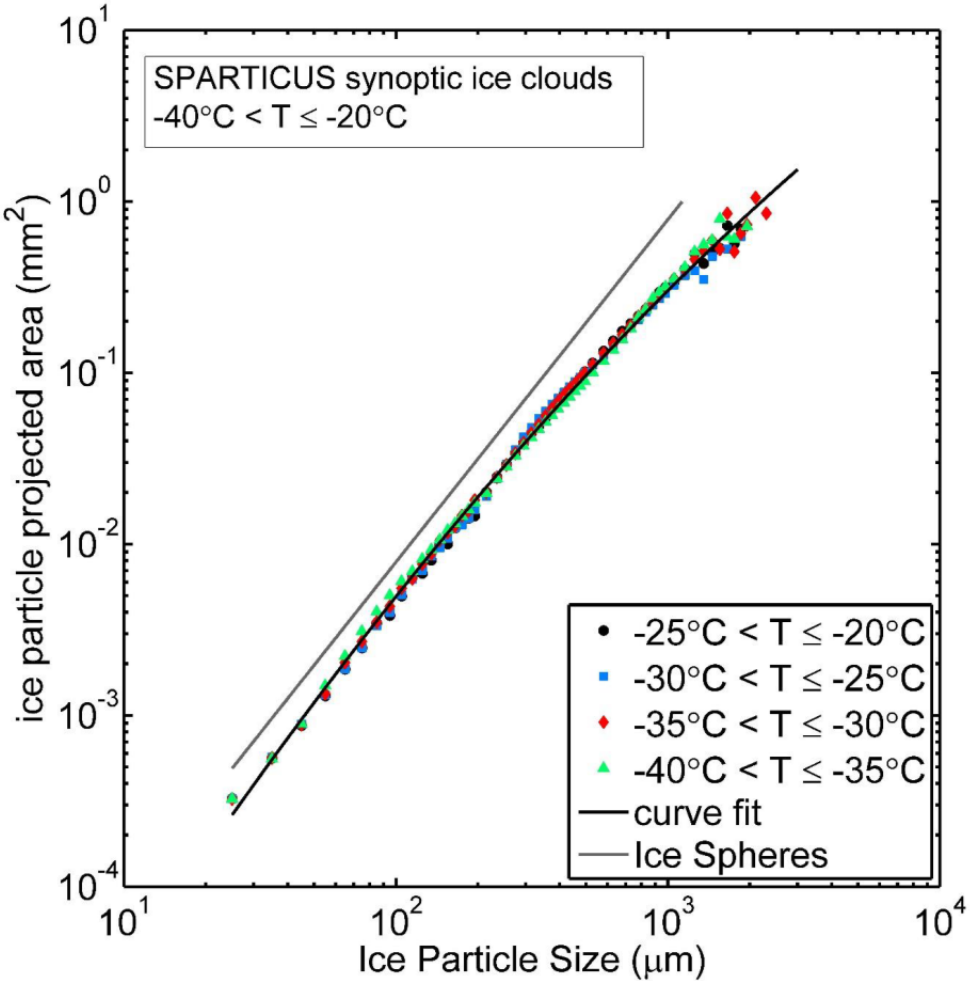

Figure 33. From Erfani and Mitchell (2015): dependence of ice particle projected area on maximum dimension D based on mean PSD within the indicated temperature regime. The black solid curve is a fit to this data.

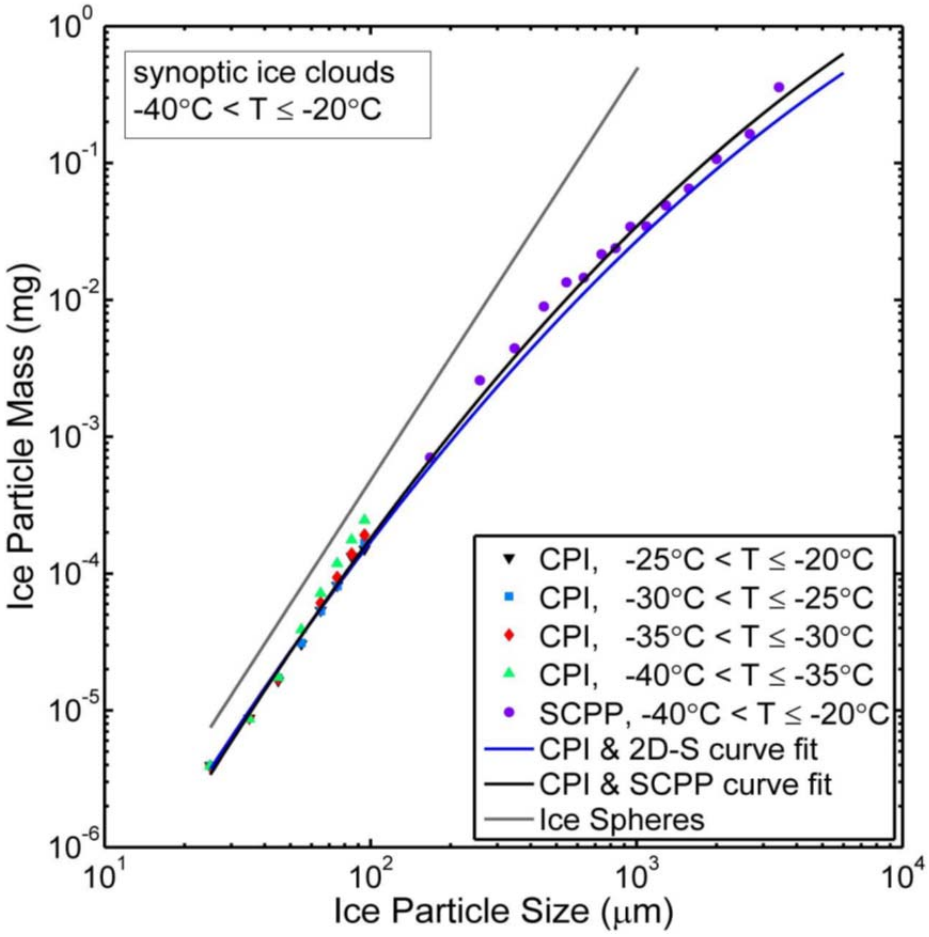

Figure 34. From Erfani and Mitchell (2015): dependence of ice particle mass on maximum dimension D for all mean PSDs sampled from synoptic cirrus clouds during SPARTICUS, where a single mean PSD is the mean of all PSD contained within a 5°C temperature interval. The two lowest curves (purple and blue) correspond to the coldest temperature intervals (i.e. -55°C < T < -60°C). The black curve is the curve fit for all synoptic mean PSD. The dashed black line for ice spheres gives the maximum possible mass for a given size D.

References

Baker, B. and R.P. Lawson: Improvement in determination of ice water content from two-dimensional particle imagery. Part I: Image-to-Mass relationships, *J. Appl. Meteor. Clim*., 45, 1282-1290, 2006.

Baker, B. and R.P. Lawson: In Situ observations of the microphysical properties of wave, cirrus, and anvil clouds. Part I: Wave Clouds, *J. Atmos. Sci*., 63, 3160-3185, 2006b.

Erfani, E. and D. Mitchell, 2015: Developing and Bounding Ice Particle Mass- and Area-dimension Expressions For Use in Atmospheric Models and Remote Sensing, submitted to *J. Geophys. Res.*.

Järvinen, E., and co-authors, 2016: Spherical ice in convective clouds. Submitted to: *J. Atmos. Sci*.

Korolev, A.: Reconstruction of the sizes of spherical particles from their shadow images. Part I: Theoretical considerations, 2007: *J. Atmos. Oceanic Technol*., 24, 376-389,

Heymsfield, A.J., and J.L. Parrish: A computational technique for increasing the effective sampling volume of the PMS two-dimensional particle size spectrometer, *J. Appl. Meteor.,* 17, 1566-1572, 1978.

Lance, S., C.A. Brock, D. Rogers, and J.A. Gordon: Water droplet calibration of a cloud droplet probe and in-flight performance in liquid, ice and mixed-phase clouds during ARCPAC, *Atmos. Meas. Tech.,* 3, 1683–1706, 2010.

Lawson, R.P.: Effects of ice particles shattering on the 2D-S probe, 2011: *Atmos. Meas. Tech*., 4, 1361-1381.

Lawson, R. P. and R. H. Cormack, 1995: Theoretical design and preliminary tests of two new particle spectrometers for cloud microphysics research. *Atmos. Res.,* **35**, 315-348.

Lawson, R. P., D. O'Connor, P. Zmarzly, K. Weaver, B. A. Baker, Q. Mo, and H. Jonsson, 2006: The 2D-S (Stereo) Probe: Design and preliminary tests of a new airborne, high speed, high-resolution particle imaging probe. *J. Atmos. Oceanic Technol.*, **23**, 1462-1477.

Muhlbauer, A., T.P. Ackerman, J. Comstock, G. Diskin, S.M. Evans, P. Lawson, and R.T. Marchand, 2013: Impact of large-scale dynamics on the microphysical properties of mid-latitude cirrus, *J. Geophys. Res. Atmos.*, 119, 3976-3996.

Muhlbauer, A., T.P. Ackerman, R.P. Lawson, S. Xie, Y. Zhang, 2015: Evaluation of cloud-resolving model simulations of midlatitude cirrus with ARM and A-train observations, *J. Geophys. Res. Atmos.*, 120, 6597-6618.